

## On the Upper-Ocean Vertical Eddy Heat Transport in the Kuroshio Extension. Part II: Effects of Air–Sea Interactions

PEIRAN YANG,<sup>a,b</sup> ZHAO JING,<sup>a,b,c</sup> BINGRONG SUN,<sup>a,b</sup> LIXIN WU,<sup>a,b</sup> BO QIU,<sup>d</sup> PING CHANG,<sup>c,e,f</sup>  
SANJIV RAMACHANDRAN,<sup>c,e</sup> AND CHUNXIN YUAN<sup>g</sup>

<sup>a</sup> *Frontiers Science Center for Deep Ocean Multispheres and Earth System and Key Laboratory of  
Physical Oceanography, Ocean University of China, Qingdao, China*

<sup>b</sup> *Pilot National Laboratory for Marine Science and Technology (Qingdao), Qingdao, China*

<sup>c</sup> *International Laboratory for High-Resolution Earth System Prediction, Texas A&M University, College Station, Texas*

<sup>d</sup> *Department of Oceanography, University of Hawai'i at Mānoa, Honolulu, Hawaii*

<sup>e</sup> *Department of Oceanography, Texas A&M University, College Station, Texas*

<sup>f</sup> *Department of Atmospheric Sciences, Texas A&M University, College Station, Texas*

<sup>g</sup> *School of Mathematical Sciences, Ocean University of China, Qingdao, China*

(Manuscript received 20 January 2021, in final form 12 August 2021)

**ABSTRACT:** Encountering of energetic ocean eddies and atmosphere storms makes the winter Kuroshio extension a hotspot for air–sea interactions. This second part investigates the regulation of vertical eddy heat transport  $Q_T$  in the winter Kuroshio extension mixed layer by different types of air–sea interactions, including the atmosphere synoptic forcing, eddy thermal feedback resulting from eddy-induced surface heat flux anomalies, and eddy current feedback from eddy current's imprint on wind stress. Atmosphere synoptic forcing modulates intraseasonal variation of  $Q_T$  by boosting its component contributed by the turbulent thermal wind balance  $Q_T^{TTW}$  during strong cooling events associated with intense winds. In addition, the magnitude of  $Q_T$  is influenced by the direction of synoptic wind stress primarily via  $Q_T^{TTW}$ , with the latter exhibiting enhancement both in the downfront- and upfront-wind forcing. Enhanced  $Q_T^{TTW}$  by the downfront-wind forcing is attributed to increased turbulent vertical viscosity and front intensity caused by the destabilizing wind-driven Ekman buoyancy flux, whereas interaction of uniform wind stress with smaller turbulent vertical viscosity at the front center than periphery (a so-called internal Ekman pumping) accounts for the increased  $Q_T^{TTW}$  in the upfront-wind forcing. The eddy thermal feedback reduces  $Q_T$  significantly through weakening the fronts. In contrast, the eddy current feedback exerts negligible influences on  $Q_T$ , although it weakens eddy kinetic energy (EKE) evidently. This is due to the much reduced effect of eddy current feedback in damping the fronts compared to EKE and also due to the compensation from Ekman pumping induced by the eddy current feedback.

**KEYWORDS:** Eddies; Ekman pumping/transport; Vertical motion; Air–sea interaction

### 1. Introduction

In the first part of this study (Yang et al. 2021, hereafter Part I), we explored the variabilities and dynamics of vertical eddy<sup>1</sup> heat transport  $Q_T$  in the winter mixed layer of the Kuroshio extension based on a 1-km regional ocean simulation. The simulated  $Q_T$  peaks around the center of the mixed layer, with its value there exhibiting pronounced intraseasonal variations. Decomposition of vertical eddy velocity based on a generalized omega equation reveals the important roles of turbulent thermal

wind (TTW) balance, net effect of frontogenesis/frontolysis, and mixed layer instability in generating  $Q_T$ . Besides being abundant in energetic ocean eddies, the winter Kuroshio extension experiences strong atmosphere synoptic variabilities, making it a hotspot for air–sea interactions (Nonaka and Xie 2003; Chelton 2004; Small et al. 2008; Cronin et al. 2010; Bishop et al. 2017). This second part is aimed to address the regulation of  $Q_T$  by such interactions and its underlying mechanisms.

Existing literature suggests that air–sea interactions can affect  $Q_T$  in a variety of ways. Passages of winter storms result in intensified surface wind stress associated with large surface heat (buoyancy) loss,<sup>2</sup> deepening the mixed layer and steepening the isopycnals. This enhances  $Q_T$  generated by mixed layer instability and frontogenesis/frontolysis as a result of increased available potential energy (Fox-Kemper et al. 2008; Thomas et al. 2008; Sasaki et al. 2014, 2017; Callies et al. 2015; McWilliams 2016; Callies and Ferrari 2018). In addition to the wind stress intensity, its direction also matters. Wind stress

<sup>1</sup> As in Part I, oceanic balanced variabilities at mesoscales and submesoscales are loosely referred to as eddies.

Denotes content that is immediately available upon publication as open access.

Supplemental information related to this paper is available at the Journals Online website: <https://doi.org/10.1175/JPO-D-21-0013.s1>.

Corresponding author: Zhao Jing, [jingzhao198763@sina.com](mailto:jingzhao198763@sina.com)

blowing along the frontal jet (the so-called downfront wind) advects dense (cold) water over the light (warm) (Thompson 2000; Thomas 2005; Thomas and Lee 2005; Mahadevan et al. 2010), exerting similar influences on the stratification and  $Q_T$  as the surface cooling and wind stirring do. The opposite is true in the upfront-wind case. Moreover, under the downfront-wind forcing, the combination of convection due to unstable stratification and nonlinear Ekman pumping drives a frontogenetic ageostrophic secondary circulation (ASC), leading to further enhancement of  $Q_T$  (Thomas and Lee 2005; Capet et al. 2008).

Although the effects of atmosphere synoptic forcing on mixed layer instability and frontogenesis/frontolysis have been relatively well investigated, its influences on TTW-induced  $Q_T$  (denoted as  $Q_T^{\text{TTW}}$ ) remain poorly assessed. Yet  $Q_T^{\text{TTW}}$  accounts for half of the entire  $Q_T$  in the mixed layer and dominates its temporal variability at intraseasonal time scales (Part I). As the turbulent vertical mixing plays a fundamental role in the TTW balance, it is very likely that  $Q_T^{\text{TTW}}$  might be strongly regulated by atmosphere synoptic forcing. In this study, we comprehensively examine the role of synoptic surface heat flux, wind stress magnitude and direction in regulating  $Q_T$  with a particular focus on  $Q_T^{\text{TTW}}$ .

Variations of heat and momentum exchanges at the air–sea interface are not simply driven by atmosphere synoptic variabilities. Sea surface temperature (SST) and current anomalies associated with ocean eddies can also leave pronounced imprints on the surface heat and momentum fluxes, which in turn feedback on eddy dynamics (Dewar and Flierl 1987; Dawe and Thompson 2006; Duhaut and Straub 2006; Small et al. 2008; Hausmann et al. 2016; Ma et al. 2016; Renault et al. 2016, 2018; Bishop et al. 2017; Shan et al. 2020a). On one hand, the eddy-induced surface heat flux anomaly damps the SST anomaly carried by eddies, acting as a key pathway for eddy available potential energy (EAPE) dissipation (referred to as the eddy thermal feedback; Hausmann et al. 2016; Ma et al. 2016; Bishop et al. 2017). On the other hand, the eddy current reduces/accelerates the wind stress blowing in the same/opposite direction, efficiently deflecting the kinetic energy from the ocean into the atmosphere (referred to as the eddy current feedback; Dawe and Thompson 2006; Duhaut and Straub 2006; Renault et al. 2016, 2018). Although both the feedbacks act to damp the eddy field, recent studies reveal their different impacts on  $Q_T$  (Ma et al. 2016; Renault et al. 2018; Shan et al. 2020a). Specifically, the magnitude of  $Q_T$  in the upper ocean is significantly weakened by the eddy thermal feedback but less sensitive to the eddy current feedback. The dynamical explanations for this difference remain elusive and will be explored in this study.

The paper is structured as follows. Section 2 presents configuration of numerical models and methodology for analysis. Regulation of  $Q_T$  by the atmosphere synoptic forcing is examined in section 3, while influences of eddy thermal and current feedbacks on  $Q_T$  are analyzed in section 4. As in Part I, we use the vertical eddy buoyancy flux  $B_f$  as a proxy for  $Q_T$  to facilitate dynamical analysis. These two quantities share very similar spatial and temporal variations because the buoyancy change is dominated by the temperature change in the Kuroshio extension (Part I; Fig. 2b). Naturally, all the effects of air–sea

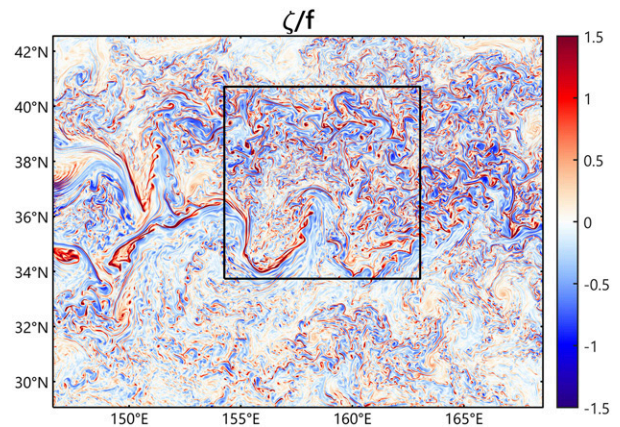


FIG. 1. A snapshot of vertical relative vorticity normalized by the Coriolis parameter  $\zeta/f$  on 21 Feb 2005 in CTRL. The outer and inner domains correspond to the domain of the 1-km ROMS simulation and the analysis region for vertical eddy heat transport, respectively.

interactions on  $B_f$  also hold for  $Q_T$ . Discussion on the implication and limitation of this study is presented in section 5. Section 6 summarizes the major conclusions.

## 2. Data and methods

### a. Numerical experiments

To analyze the regulation of  $B_f$  by different forms of air–sea interactions (i.e., atmosphere synoptic forcing, eddy thermal and current feedbacks), three numerical simulations are carried out based on the Regional Ocean Modeling System (ROMS; Haidvogel et al. 2000; Shchepetkin and McWilliams 2005) configured over the winter Kuroshio extension (146.6°–168.5°E, 29°–42.6°N; Fig. 1) with ~1-km horizontal resolution and 65 terrain following vertical levels. The vertical grid size is less than 6 m in the upper 100 m. The control run (CTRL) is identical to the one used in Part I. It is a standard ocean simulation with the atmosphere forcing provided by the Climate Forecast System Reanalysis (CFSR; Saha et al. 2010) on a 6-hourly grid of 0.5° resolution based on the bulk formula (Large and Yeager 2004). The turbulent vertical mixing is parameterized by a  $K$ -profile parameterization (KPP) turbulent mixing closure scheme (Large et al. 1994). A biharmonic horizontal Smagorinsky-like mixing scheme (Smagorinsky 1963; Griffies and Hallberg 2000) is used for momentum, whereas no horizontal mixing parameterization for tracers is applied. The boundary and initial conditions are obtained from a parent ROMS simulation configured over the North Pacific (99°–270°E, 3.6°–66°N) with 9-km horizontal resolution and 50 vertical levels. The effects of atmosphere synoptic forcing, eddy thermal and current feedbacks are all included in CTRL, although the eddy thermal and current feedbacks tend to be moderately overestimated due to the lack of atmosphere’s adjustment to eddy-induced SST and current anomalies (Renault et al. 2016; Yang et al. 2018), which is acceptable for our qualitative analysis. Accurate

representation of these feedbacks requires coupled simulations that are currently challenging at 1-km resolution.

The second run has the same setting as CTRL except that the wind stress is computed based on the surface wind alone instead of the vector difference between surface wind and current. This modified wind stress thus excludes the eddy current feedback and the second run is referred to as the no-current feedback (NCFB) run. The third run shares the same initial and boundary conditions as CTRL but is forced by the spatially smoothed 3-hourly averaged surface momentum, heat and freshwater fluxes derived from CTRL. A  $200 \times 200 \text{ km}^2$  running-mean is used to smooth out the eddy's imprints on surface fluxes, in which case both the eddy thermal and current feedbacks are largely suppressed. We refer to this third run as the no-eddy feedback (NEFB) simulation. Comparisons among CTRL, NCFB and NEFB enable us to isolate the regulation of  $B_f$  by different forms of air–sea interactions.

All the three experiments are initialized on 30 September 2004 and integrated for 6 months with 3-hourly averaged velocity, temperature, salinity, and individual diagnostic terms in momentum and tracer equations stored. After 2-month spinup, variables from 1 December to 31 March in an inner domain of  $154.3^\circ\text{--}163.0^\circ\text{E}$ ,  $33.7^\circ\text{--}40.7^\circ\text{N}$  (Fig. 1) are used for analyses. As in Part I, a low-pass filter with a cutoff frequency of 0.8 the local inertial frequency is applied to all variables to eliminate the interference from unbalanced dynamics (e.g., internal waves).

#### b. Turbulent thermal wind balance

The TTW balance (Gula et al. 2014) extends the thermal wind balance (Vallis 2006) by taking into consideration the important role of turbulent vertical mixing in the momentum balance in the mixed layer:

$$fv_a = -\frac{\partial}{\partial z} \left( K_m \frac{\partial u_a}{\partial z} \right) - \frac{\partial}{\partial z} \left( K_m \frac{\partial u_g}{\partial z} \right), \quad (1a)$$

$$fu_a = \frac{\partial}{\partial z} \left( K_m \frac{\partial v_a}{\partial z} \right) + \frac{\partial}{\partial z} \left( K_m \frac{\partial v_g}{\partial z} \right), \quad (1b)$$

with the boundary conditions<sup>3</sup>

$$\rho_0 K_m \left( \frac{\partial \mathbf{v}_g}{\partial z} + \frac{\partial \mathbf{v}_a}{\partial z} \right) \Big|_{z=0} = \boldsymbol{\tau}, \quad (1c)$$

$$\rho_0 K_m \left( \frac{\partial \mathbf{v}_g}{\partial z} + \frac{\partial \mathbf{v}_a}{\partial z} \right) \Big|_{z=-\infty} = 0, \quad (1d)$$

where  $\mathbf{v}_g = (u_g, v_g)$  is the geostrophic velocity and  $\mathbf{v}_a = (u_a, v_a) = (u - u_g, v - v_g)$  is the ageostrophic horizontal velocity,  $f$  is the Coriolis parameter,  $\rho_0$  is the reference density set as  $1025 \text{ kg m}^{-3}$ ,  $K_m$  is the turbulent vertical viscosity parameterized by the KPP scheme (Large et al. 1994), and  $\boldsymbol{\tau} = (\tau_x, \tau_y)$  is the surface wind stress. The lower

boundary condition Eq. (1d) is posed as a no-stress condition following Cronin and Kessler (2009) and Wenegrat and McPhaden (2016).

The horizontal ageostrophic flows in the TTW balance can be treated as a linear superposition of components driven by wind stress,<sup>4</sup> denoted as  $\mathbf{v}_E = (u_E, v_E)$ , and by geostrophic shear  $\partial \mathbf{v}_g / \partial z$  in the presence of turbulent vertical viscous effects, denoted as  $\mathbf{v}_S = (u_S, v_S)$ . The former  $\mathbf{v}_E$  is identical to the classical wind-driven Ekman flow apart from a vertically varying rather than constant  $K_m$ :

$$fv_E = -\frac{\partial}{\partial z} \left( K_m \frac{\partial u_E}{\partial z} \right), \quad (2a)$$

$$fu_E = \frac{\partial}{\partial z} \left( K_m \frac{\partial v_E}{\partial z} \right), \quad (2b)$$

with the boundary conditions

$$\rho_0 K_m \frac{\partial \mathbf{v}_E}{\partial z} \Big|_{z=0} = \boldsymbol{\tau}, \quad (2c)$$

$$\rho_0 K_m \frac{\partial \mathbf{v}_E}{\partial z} \Big|_{z=-\infty} = 0. \quad (2d)$$

The latter  $\mathbf{v}_S$ , essentially induced by the turbulent vertical mixing of geostrophic momentum, is governed by the following equations:

$$fv_S = -\frac{\partial}{\partial z} \left( K_m \frac{\partial u_S}{\partial z} \right) - \frac{\partial}{\partial z} \left( K_m \frac{\partial u_g}{\partial z} \right), \quad (3a)$$

$$fu_S = \frac{\partial}{\partial z} \left( K_m \frac{\partial v_S}{\partial z} \right) + \frac{\partial}{\partial z} \left( K_m \frac{\partial v_g}{\partial z} \right), \quad (3b)$$

with the boundary conditions

$$\rho_0 K_m \frac{\partial \mathbf{v}_S}{\partial z} \Big|_{z=0} = -\rho_0 K_m \frac{\partial \mathbf{v}_g}{\partial z} \Big|_{z=0}, \quad (3c)$$

$$\rho_0 K_m \left( \frac{\partial \mathbf{v}_g}{\partial z} + \frac{\partial \mathbf{v}_S}{\partial z} \right) \Big|_{z=-\infty} = 0. \quad (3d)$$

Equations (2) and (3) can be solved using the relaxation method (Ortega and Rheinboldt 2014) with the values of  $K_m$ ,  $\mathbf{v}_g$ , and  $\boldsymbol{\tau}$  obtained from the model output. To facilitate the numerical computation, we replace the lower boundary  $z = -\infty$  with a finite depth  $h_b$  of 500 m that is well below the surface boundary layer. Sensitivity tests suggest that using a larger depth for the lower boundary does not result in any noticeable difference in the solutions, lending support to our choice.

Once the solutions of  $\mathbf{v}_E$  and  $\mathbf{v}_S$  are obtained, their associated vertical velocity can be respectively computed as

<sup>3</sup> Strictly speaking, Eq. (1c) should not be applied to the sea surface but to the depth where effects of molecular processes and surface roughness elements become negligible. A similar argument holds for Eqs. (2c) and (3c).

<sup>4</sup> It should be noted that the definition of ageostrophic flows in the TTW balance is not unique. In some other literature (e.g., Wenegrat et al. 2018), the TTW ageostrophic flow is defined as  $\mathbf{v}_S$  with  $\mathbf{v}_E$  excluded.

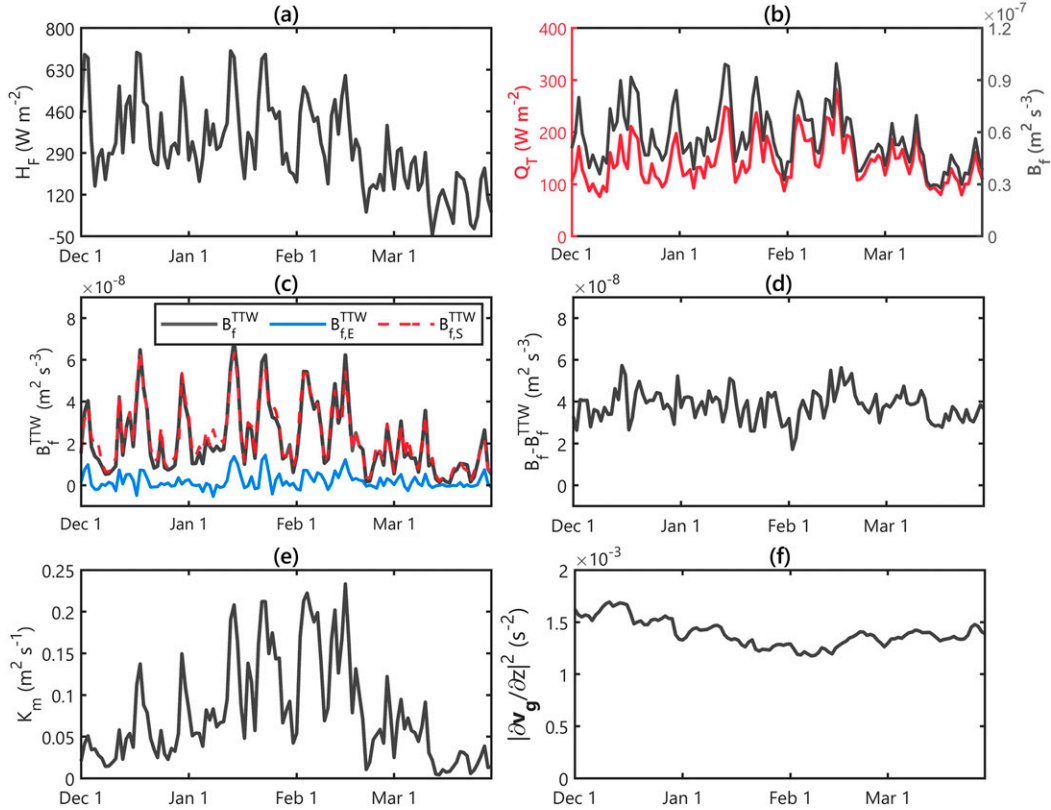


FIG. 2. Time series of (a)  $\langle H_F \rangle_s$ ; (b)  $\langle Q_T \rangle_s$  (red) and  $\langle B_f \rangle_s$  (black); (c)  $\langle B_f^{TTW} \rangle_s$  (black),  $\langle B_{f,E}^{TTW} \rangle_s$  (blue), and  $\langle B_{f,S}^{TTW} \rangle_s$  (red); (d)  $\langle B_f - B_f^{TTW} \rangle_s$ ; (e)  $\langle K_m \rangle_s$ ; and (f)  $\langle |\partial \mathbf{v}_g / \partial z|^2 \rangle_s$ , all at 60 m. The values are derived from NEFB.

$$w_E = \frac{1}{f} \left[ \frac{1}{\rho_0} \nabla_H \times \boldsymbol{\tau} \cdot \mathbf{k} - \left( \frac{\partial}{\partial x} K_m \frac{\partial v_E}{\partial z} - \frac{\partial}{\partial y} K_m \frac{\partial u_E}{\partial z} \right) \right], \quad (4)$$

and

$$w_S = -\frac{1}{f} \left[ \frac{\partial}{\partial x} K_m \frac{\partial (v_S + v_g)}{\partial z} - \frac{\partial}{\partial y} K_m \frac{\partial (u_S + u_g)}{\partial z} \right], \quad (5)$$

where  $\mathbf{k}$  is the unit vector in  $z$  direction, and  $\nabla_H = (\partial/\partial x, \partial/\partial y)$ . Equations (4) and (5) provide a linear decomposition of vertical velocity driven by wind stress and vertical mixing of geostrophic momentum under the TTW balance. Note that in the classical Ekman model (Ekman 1905; Vallis 2006) adopting a horizontally homogeneous  $K_m$ ,  $w_E$  is generated solely by the wind stress curl and equal to the Ekman pumping velocity  $w_\tau = (f\rho_0)^{-1} \nabla_H \times \boldsymbol{\tau} \cdot \mathbf{k}$  at the Ekman layer base where the second term on the rhs of Eq. (4) vanishes.

### c. Generalized geostrophic momentum approximation (G-GMA) omega equation

To uncover the underlying dynamics responsible for the regulation of  $B_f$  by different forms of air–sea interactions, the G-GMA omega equation derived and proved effective in Part I is used to decompose vertical velocity associated with different mechanisms:

$$f^2 \frac{\partial^2 w}{\partial z^2} + \langle N^2 \rangle_s \nabla_H^2 w = F_{qg} + F_{ag} + F_{vm} + F_{hm} + F_{vb}, \quad (6)$$

where  $N^2$  is the squared buoyancy frequency and  $\langle \rangle_s$  is the spatial average in the inner domain (154.3°–163.0°E, 33.7°–40.7°N). The forcing terms on the rhs of Eq. (6) correspond sequentially to the effects of geostrophic deformation, ageostrophic advection in the GMA regime, vertical mixing of momentum, horizontal mixing of momentum and vertical mixing of buoyancy. The readers are referred to the appendix or to Part I for explicit expressions of the forcing terms in Eq. (6).

Due to the linear nature of Eq. (6), its solution,  $w^o$ , can be represented as the superposition of six independent components with distinct dynamics, i.e.,

$$w^o = w^{qg} + w^{ag} + w^{vm} + w^{hm} + w^{vb} + w^{bry}. \quad (7)$$

The solutions  $w^{qg}$ ,  $w^{ag}$ ,  $w^{vm}$ ,  $w^{hm}$ , and  $w^{vb}$  represent contributions from individual rhs forcing terms, while the solution  $w^{bry}$  represents contribution from the boundary conditions. The G-GMA omega equation is solved over the inner domain and 0–530 m in depth using successive overrelaxation method with Chebyshev acceleration (Press et al. 1992; Allen et al. 2001).

### d. Computation of vertical eddy buoyancy flux

The value of  $B_f$  is computed as

$$B_f = w'b',$$

where  $b = -g\rho_0^{-1}(\rho - \rho_0)$  is the buoyancy and the prime represents eddy anomalies defined as perturbations from the zonal



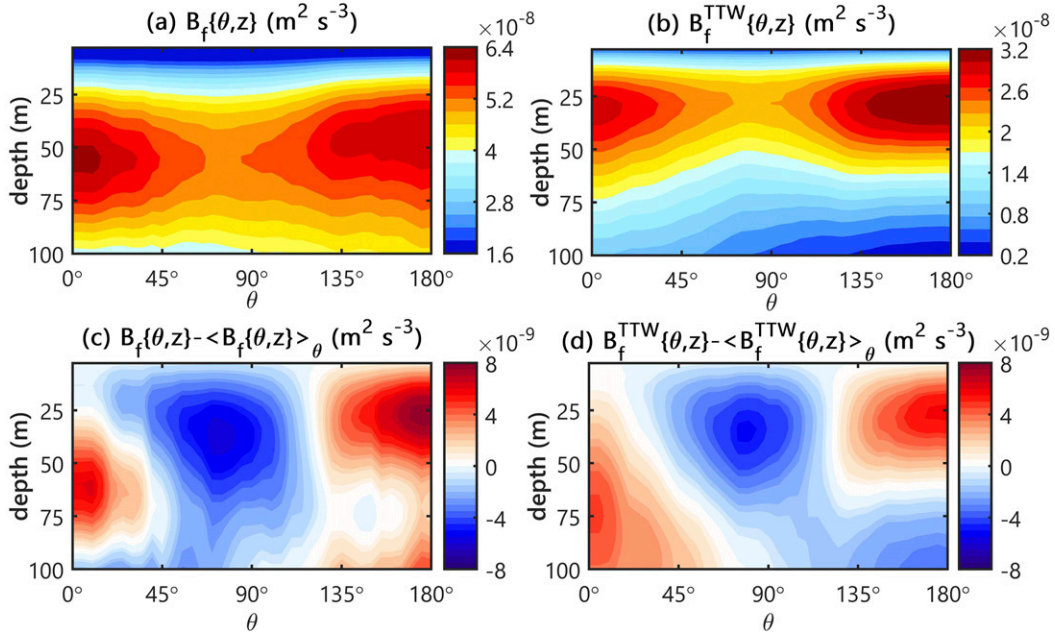


FIG. 3. Distributions of (a)  $B_f\{\theta, z\}$ , (b)  $B_f^{\text{TTW}}\{\theta, z\}$ , (c)  $B_f\{\theta, z\} - \langle B_f\{\theta, z\} \rangle_\theta$ , and (d)  $B_f^{\text{TTW}}\{\theta, z\} - \langle B_f^{\text{TTW}}\{\theta, z\} \rangle_\theta$  in the upper 100 m. The values are derived from NEFB.

average. As in Part I, we approximate  $w'$  by  $w$  to facilitate dynamical analysis. Such an approximation has nearly no influence on the variability of  $B_f$  due to the smallness of zonal mean  $w$  (Part I).

Before ending this section, we briefly summarize the conclusions in Part I that underpin the analysis in this study. In the mixed layer, both the mean value and variability of  $B_f$  are mainly accounted for by the contributions from the geostrophic deformation  $B_f^{\text{ge}} = w^{\text{ge}}b'$  and vertical mixing of momentum  $B_f^{\text{vm}} = w^{\text{vm}}b'$ . The net effect of frontogenesis/frontolysis and mixed layer instability contribute comparably to  $B_f^{\text{ge}}$ . The value of  $B_f^{\text{vm}}$  is almost identical to the vertical eddy buoyancy flux derived from the TTW balance  $B_f^{\text{TTW}} = (w_E + w_S)b'$ , but is evidently smaller than that from the model proposed by Garrett and Loder (1981) who neglected the first term on the rhs of Eq. (1) (see Part I for more details). The two quantities,  $B_f^{\text{vm}}$  and  $B_f^{\text{TTW}}$ , are used interchangeably in this study.

### 3. Regulation of vertical eddy heat transport by atmosphere synoptic forcing

Simulation results in NEFB are used to evaluate the regulation of  $B_f$  by atmosphere synoptic forcing as the eddy thermal and current feedbacks are removed in this simulation. As mentioned in the introduction, the effects of atmosphere synoptic forcing can be divided into three factors, i.e., surface heat flux and wind stress magnitude and direction. In the winter Kuroshio extension, the former two factors are tightly correlated as strong wind increases heat loss at the sea surface, working in concert to enhance the turbulent vertical mixing in the upper ocean. For this sake, we treat these two factors as a whole and use

the surface heat flux (defined positive upward) as their representative.

#### a. Effects of surface heat flux/wind stress magnitude

Figures 2a and 2b display the time series of region-averaged ( $154.3^\circ\text{E}$ – $163.0^\circ\text{E}$ ,  $33.7^\circ\text{N}$ – $40.7^\circ\text{N}$ ) surface heat flux  $\langle H_F \rangle_s$  and  $\langle B_f \rangle_s$  at its peaking depth ( $\sim 50$  m) in NEFB. The time series of  $\langle B_f \rangle_s$  generally follows that of  $\langle H_F \rangle_s$  especially at intraseasonal time scales, with a correlation coefficient of 0.79. As shown in Figs. 2c and 2d, the tight association is mainly attributed to the strong regulation of TTW balance by  $\langle H_F \rangle_s$ . The correlation coefficient between  $\langle H_F \rangle_s$  and  $\langle B_f^{\text{TTW}} \rangle_s$  at 50 m reaches up to 0.86, whereas the value decreases to  $-0.11$  for  $\langle H_F \rangle_s$  and  $\langle B_f - B_f^{\text{TTW}} \rangle_s$ . The relatively low correlation between  $\langle H_F \rangle_s$  and  $\langle B_f - B_f^{\text{TTW}} \rangle_s$  does not mean insignificant influences of  $\langle H_F \rangle_s$  on frontogenesis/frontolysis and mixed layer instability, as the mixed layer depth, a key factor in these mechanisms (Fox-Kemper et al. 2008; McWilliams 2016), may rely more on the accumulated effect of  $\langle H_F \rangle_s$  rather than on its instantaneous impact. Given that the regulation of frontogenesis/frontolysis and mixed layer instability by  $\langle H_F \rangle_s$  has been well documented elsewhere (e.g., Callies et al. 2015; Sasaki et al. 2017; Callies and Ferrari 2018), we will focus on understanding the tight association between  $\langle B_f^{\text{TTW}} \rangle_s$  and  $\langle H_F \rangle_s$  in the following analysis.

Following section 2b, we decompose  $B_f^{\text{TTW}}$  into components driven by wind stress  $B_{f,E}^{\text{TTW}} = w_E b'$  and vertical mixing of geostrophic momentum  $B_{f,S}^{\text{TTW}} = w_S b'$ , respectively. The latter is found to make dominant contribution to  $\langle B_f^{\text{TTW}} \rangle_s$  and its intraseasonal variations (Fig. 2c). Assuming  $\nabla_H b' \approx \nabla_H b'$ , an

<sup>5</sup> Locally,  $B_{f,E}^{\text{TTW}}$  could be still important, as will be shown in section 3b.

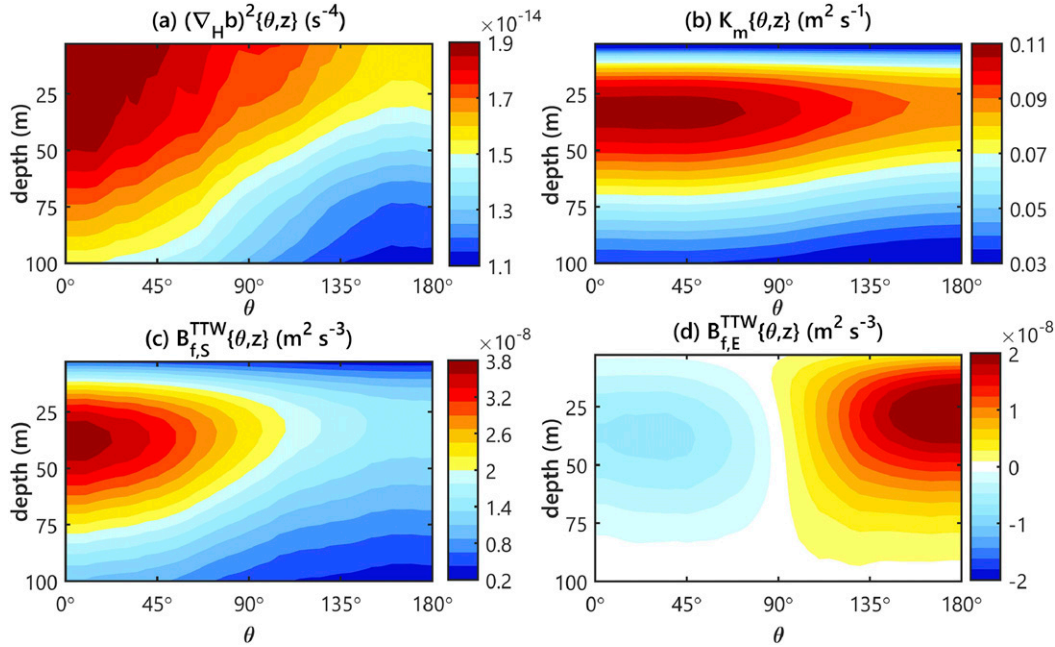


FIG. 4. Distributions of (a)  $(\nabla_H b)^2\{\theta, z\}$ , (b)  $K_m\{\theta, z\}$ , (c)  $B_{f,S}^{TTW}\{\theta, z\}$ , and (d)  $B_{f,E}^{TTW}\{\theta, z\}$  in the upper 100 m. The values are derived from NEFB.

approximation of high level of accuracy,  $\langle B_{f,S}^{TTW} \rangle_s$  can be expressed after some manipulations as:

$$\langle B_{f,S}^{TTW} \rangle_s = -\frac{1}{A} \oint \frac{1}{f} b' K_m \frac{\partial \mathbf{v}_s + \mathbf{v}_g}{\partial z} \cdot d\mathbf{l} + \left\langle K_m \frac{\partial \mathbf{v}_s + \mathbf{v}_g}{\partial z} \cdot \frac{\partial \mathbf{v}_g}{\partial z} \right\rangle_s, \quad (8)$$

where  $A$  is the area of the computational domain and  $d\mathbf{l}$  is the line element along the boundaries. The first term on the rhs of Eq. (8) is the boundary effect that is negligible for our analysis domain. The second term is equal to the product of  $K_m$ , geostrophic shear and total shear  $\partial(\mathbf{v}_s + \mathbf{v}_g)/\partial z$ . As suggested by Eq. (3) and Wenegrat and McPhaden (2016),  $\partial \mathbf{v}_s / \partial z$  depends linearly on  $\partial \mathbf{v}_g / \partial z$ . We thus expect that  $K_m \partial(\mathbf{v}_s + \mathbf{v}_g) / \partial z$  can be approximated as  $\alpha(z) K_m \partial \mathbf{v}_g / \partial z$  with  $\alpha(z)$  a nonnegative coefficient. Under such approximation,  $\langle B_{f,S}^{TTW} \rangle_s$  should increase with  $\langle K_m \rangle_s$  and  $\langle |\partial \mathbf{v}_g / \partial z|^2 \rangle_s$ , which is consistent with the idea that the stronger the front and turbulent vertical mixing, the stronger ASC under the TTW balance (e.g., McWilliams et al. 2015).

It is found that the temporal variation of  $\langle B_{f,S}^{TTW} \rangle_s$  at the intraseasonal time scales is dominated by that of  $\langle K_m \rangle_s$  (Fig. 2e) with their correlation coefficient being 0.91, whereas the variability of  $\langle |\partial \mathbf{v}_g / \partial z|^2 \rangle_s$  is much weaker and plays a minor role (Fig. 2f). This explains the significant regulation of  $\langle B_{f,S}^{TTW} \rangle_s$  and further  $\langle B_f^{TTW} \rangle_s$  by  $\langle H_F \rangle_s$  as the value of  $K_m$  in the winter mixed layer is largely controlled by the surface heat loss and wind stirring (Large et al. 1994; Marshall and Schott 1999). Indeed, the correlation coefficient between  $\langle H_F \rangle_s$  and  $\langle K_m \rangle_s$  at 50 m reaches 0.78.

#### b. Downfront versus upfront wind

To explore how the wind stress direction affects  $B_f$ , we evaluate the dependence of  $B_f$  on the vectorial angle  $\theta$

between wind stress and fronts. The frontal direction is defined as the direction of  $\mathbf{k} \times \nabla_H b^z$ , with the superscript  $z$  denoting the vertical average within the mixed layer. By definition, the wind stress blowing in the downfront (upfront) direction corresponds to  $\theta = 0^\circ$  ( $\theta = 180^\circ$ ), while the cross-front directed wind stress (either pointing to the dense or buoyant side) corresponds to  $\theta = 90^\circ$ . The values of  $|\tau|\{\theta\}$  and  $H_F\{\theta\}$ , obtained by calculating the compositing average of  $|\tau|$  and  $H_F$  for different bins of  $\theta$  with a bin size of  $5^\circ$ , are almost constant (Fig. S1 in the online supplemental material). This guarantees that the effect of wind stress direction on  $B_f$  is not conflated with that of heat flux/wind stress magnitude.

The value of  $B_f\{\theta, z\}$  in the mixed layer exhibits enhancement both in the downfront- and upfront-wind cases (Fig. 3a). Such  $\theta$ -dependent pattern is mainly ascribed to  $B_f^{TTW}\{\theta, z\}$  (Fig. 3b). Specifically, the pattern correlation coefficient between  $B_f\{\theta, z\} - \langle B_f\{\theta, z\} \rangle_\theta$  and  $B_f^{TTW}\{\theta, z\} - \langle B_f^{TTW}\{\theta, z\} \rangle_\theta$  in the upper 100 m reaches up to 0.72 (Figs. 3c,d), where  $\langle \cdot \rangle_\theta$  represents the average over all the values of  $\theta$ . The intensified  $B_f^{TTW}\{\theta, z\}$  in the downfront-wind case is mainly ascribed to  $B_{f,S}^{TTW}\{\theta, z\}$  that reaches its maximum around  $\theta = 0^\circ$  and decreases monotonically with the increment of  $\theta$  (Fig. 4c). Such a pattern of  $B_{f,S}^{TTW}\{\theta, z\}$  is expected as wind stress blowing in the downfront direction weakens the stratification through the destabilizing wind-driven Ekman buoyancy flux (Thomas and Lee 2005) and meanwhile triggers frontogenesis (Thompson 2000; Thomas 2005; Thomas and Lee 2005). The former energizes turbulent vertical mixing and the latter enhances the front intensity. These two effects work jointly to induce a stronger ASC and thus promote  $B_{f,S}^{TTW}$  for the downfront wind forcing, whereas the opposite is true for the upfront-wind forcing, as evidenced by the decreasing trends of  $(\nabla_H b)^2\{\theta, z\}$  and  $K_m\{\theta, z\}$  with  $\theta$  (Figs. 4a,b).

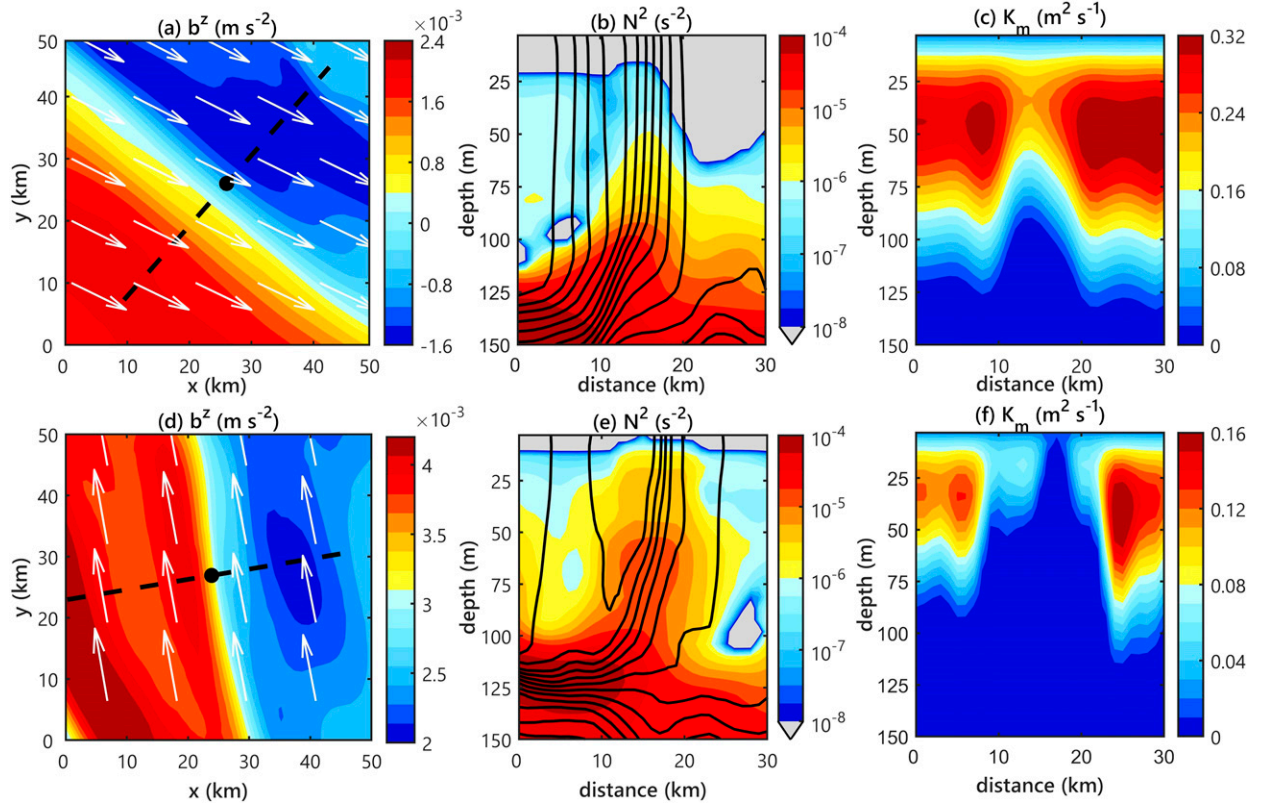


FIG. 5. (a) Snapshot of  $b^z$  (color) for a front undergoing downfront-wind forcing, with the direction of wind stress indicated by white arrows. Cross-front sections, marked by dashed black line in (a), of (b)  $N^2$  and (c)  $K_m$  with contours denoting  $b$ . (d)–(f) As in (a)–(c), but for a front undergoing upfront-wind forcing. The gravitational unstable stratification is filled with gray. The values are derived from NEFB.

The enhanced  $B_f^{\text{TTW}}\{\theta, z\}$  in the upfront-wind case is caused by  $B_{f,E}^{\text{TTW}}\{\theta, z\}$ . The latter is characterized by an asymmetric dipole, exhibiting large positive and small negative values when wind stress blows in the upfront and downfront directions, respectively (Fig. 4d). The dipolar structure of  $B_{f,E}^{\text{TTW}}\{\theta, z\}$  can be understood on the basis of the regulation of wind-driven Ekman flows by  $K_m$ . Even though the wind stress is almost uniform at the frontal scale as in NEFB, vertical motions could still be generated due to the horizontally inhomogeneous  $K_m$ . Figure 5 displays cross-front sections of  $K_m$  and  $N^2$  for some representative fronts undergoing downfront- and upfront-wind forcing, respectively. The most prominent feature is the enhanced  $N^2$  and reduced  $K_m$  at the front center than periphery, regardless of the wind stress direction. Accordingly,  $\mathbf{v}_E$  decays and rotates more rapidly with depth at the front center than periphery (Wenegrat and McPhaden 2016). Moreover, as the vertically integrated transport by  $\mathbf{v}_E$  is solely determined by the surface wind stress through the relation  $\int_{-h_b}^0 \mathbf{v}_E dz = (\boldsymbol{\tau} \times \mathbf{k}) / (f\rho_0)$ , more rapid decay and rotation of  $\mathbf{v}_E$  with depth correspond to a stronger cross-front component of  $\mathbf{v}_E$  (denoted as  $v_{E,n}$ ) at the sea surface in both the downfront- and upfront-wind forcing. In the upfront-wind case, such regulation of  $K_m$  on  $\mathbf{v}_E$  results in surface divergence (convergence) on the light (dense) side of the front, with the opposite occurring at the depth where the sign of  $v_{E,n}$  is reversed at the front center but remains unchanged at the periphery. This produces upwelling and downwelling on light and

dense sides of the front respectively, accounting for the positive  $B_{f,E}^{\text{TTW}}\{\theta, z\}$  under the upfront-wind forcing. In the downfront-wind case, the situation is similar except that the direction of  $\mathbf{v}_E$  is entirely reversed. Correspondingly, the upwelling and downwelling reside on the dense and light sides of the front, respectively, leading to negative  $B_{f,E}^{\text{TTW}}\{\theta, z\}$ . Figure 6 presents a schematic summarizing the above mechanism.

On one hand, the reduced  $K_m$  at the front center than periphery is expected in the upfront-wind case as both  $B_f$  and wind-driven Ekman buoyancy flux act to restratify the front and thus reduce  $K_m$ . On the other hand, similar cross-front structure of  $K_m$  in the downfront-wind case suggests that the restratification by  $B_f$  overwhelms the destratification by the wind-driven Ekman buoyancy flux, which is probably due to the short persistency of the alignment between wind and frontal jet (Mahadevan et al. 2010). In fact, the decorrelation time scale of  $\theta$  is only about 9 h in NEFB as a result of rapidly changing of wind stress and fronts direction (not shown). This should be distinguished from the idealized simulation results in Thomas and Lee (2005) and Thomas and Ferrari (2008) who prescribed a wind stress perpetually blowing in the downfront direction. To examine whether its dominant influence of  $B_f$  over wind-driven Ekman buoyancy flux on  $N^2$  and  $K_m$  in the downfront-wind case is universal, we compute the compositing average of  $N^{2z}$ ,  $(\partial \mathbf{v} / \partial z)^2$ , and  $K_m^z$  for different bins of  $(\nabla_H b^z)^2$ , only counting samples with  $0 < \theta < 30^\circ$ . As shown



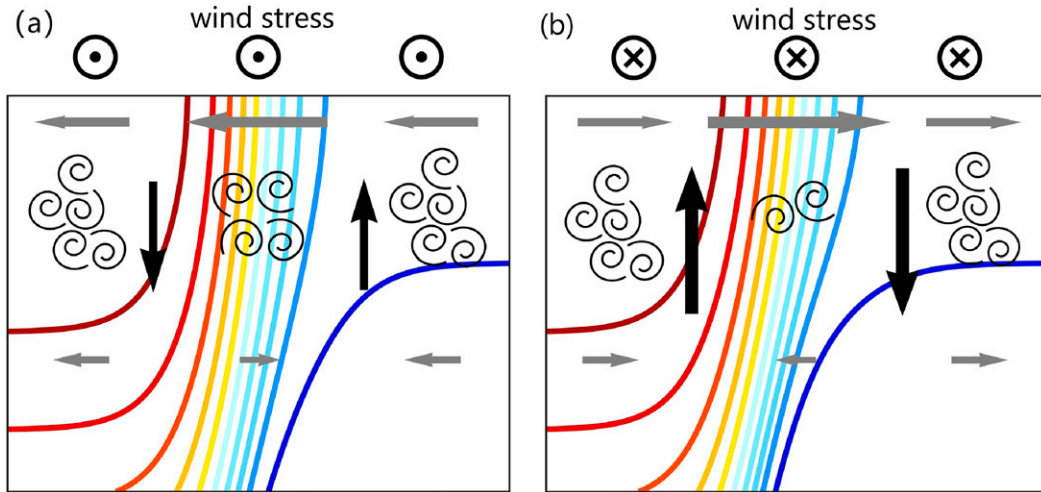


FIG. 6. Schematics of the internal Ekman pumping under the (a) downfront- and (b) upfront-wind forcing with reduced  $K_m$  at the front center than periphery. In NEFB, the surface wind stress is almost uniform at the frontal scale due to the absence of eddy current's imprint on wind stress. However,  $\mathbf{v}_E$  is not horizontally homogeneous as the reduced  $K_m$  at the front center makes  $\mathbf{v}_E$  decay and rotate more rapidly with depth there. This results in larger magnitude of  $v_{E,n}$  at the front center than periphery at the sea surface. The more rapid rotation of  $\mathbf{v}_E$  with depth at the front center than periphery means there must be a depth at which the sign of  $v_{E,n}$  becomes opposite to its surface value at the front center but remains unchanged at the periphery. The different vertical profiles of  $v_{E,n}$  between the front center and periphery result in horizontal divergence/convergence and generate vertical motions due to the incompressibility of the seawater. The vertical motions are stronger in the upfront- than downfront-wind case. This is because the wind-driven Ekman buoyancy flux and  $B_f$  work in concert to restratify the front under the upfront-wind forcing but work against each other under the downfront-wind forcing. Correspondingly, the reduced  $K_m$  at the front center is more evident in the upfront- than downfront-wind case.

in Fig. 7a,  $K_m^z$  decreases monotonically as  $(\nabla_H b^z)^2$  increases in the downfront-wind case. Such a pattern of  $K_m^z$  is due to the enhanced  $N^{2z}$  with the increment of  $(\nabla_H b^z)^2$  (Fig. 7b), whereas  $(\partial v / \partial z)^{z2}$ , becoming stronger with the increased  $(\nabla_H b^z)^2$  as expected, partially offsets the influence of  $N^{2z}$  on  $K_m^z$  (Fig. 7c). This confirms the dominance of  $B_f$ -induced restratification over the destratification by the wind-driven Ekman buoyancy flux. Moreover, as  $B_f$  and wind-driven Ekman buoyancy flux work in concert to restratify fronts under the upfront-wind forcing but compete against each other under the downfront-wind forcing, the increasing rate of  $N^{2z}$  with  $(\nabla_H b^z)^2$  is larger in the upfront-wind than downfront-wind case (Fig. 7b). Correspondingly,  $K_m^z$  decreases more rapidly with the increased  $(\nabla_H b^z)^2$  in the upfront-wind than downfront-wind case (Fig. 7a), as the dependence of  $(\partial v / \partial z)^{z2}$  on  $(\nabla_H b^z)^2$  is insensitive to the wind stress direction relative to the frontal jet (Fig. 7c). This makes the contrast of  $K_m$  between the front center and periphery more evident under the upfront-wind than downfront-wind forcing (Fig. 5), explaining the asymmetric dipolar structure of  $B_{f,E}^{\text{TTW}}\{\theta, z\}$  (Figs. 4d and 6).

#### 4. Regulation of vertical eddy heat transport by eddy thermal and current feedbacks

##### a. Eddy thermal feedback

The influence of eddy thermal feedback on  $B_f$  is evaluated by comparing the results in NCFB and NEFB. The eddy

thermal feedback acts as an efficient dissipator for EAPE (Ma et al. 2016; Yang et al. 2019; Shan et al. 2020a), leading to weakened fronts in the upper ocean (Fig. 8a). The time mean  $\langle (\nabla_H b)^2 \rangle_s$  [denoted as  $\langle (\nabla_H b)^2 \rangle_{s,t}$  henceforth] in the upper 100 m is 34.2% smaller in NCFB than NEFB. Qualitatively consistent with the findings by Ma et al. (2016), Yang et al. (2019) and Shan et al. (2020a), the magnitude of  $\langle B_f \rangle_{s,t}$  at its peaking depth is reduced by 11.7% in response to the eddy thermal feedback (Fig. 9a). Decomposition of  $B_f$  based on the G-GMA omega equation as in Part I reveals the weakened  $\langle B_f \rangle_{s,t}$  in NCFB than NEFB is equally ascribed to the reduction of  $\langle B_f^{\text{qg}} \rangle_{s,t}$  and  $\langle B_f^{\text{vm}} \rangle_{s,t}$  (Figs. 9b,c), whereas the remaining components play a minor or negligible role. It thus suggests that the effects of frontogenesis/frontolysis, mixed layer instability, and TTW balance are all weakened by the eddy thermal feedback.

The front intensity is a key factor controlling the magnitude of  $B_f$  generated by frontogenesis/frontolysis, mixed layer instability, and TTW balance (Fox-Kemper et al. 2008; Gula et al. 2014; McWilliams 2016, 2017). However, the difference of  $\langle B_f \rangle_{s,t}$  between NCFB and NEFB is evidently smaller than the difference of  $\langle (\nabla_H b)^2 \rangle_{s,t}$ . Such discrepancy is mainly due to the restratification by  $B_f$  and its negative feedback onto  $B_f$  itself. The smaller magnitude of  $B_f$  in NCFB causes weaker stratification in the upper ocean (Fig. 8b). On one hand, the weakened stratification in NCFB increases the mixed layer depth ( $H$ ), acting to enhance  $B_f$  induced by the mixed layer instability and frontogenesis/frontolysis, as



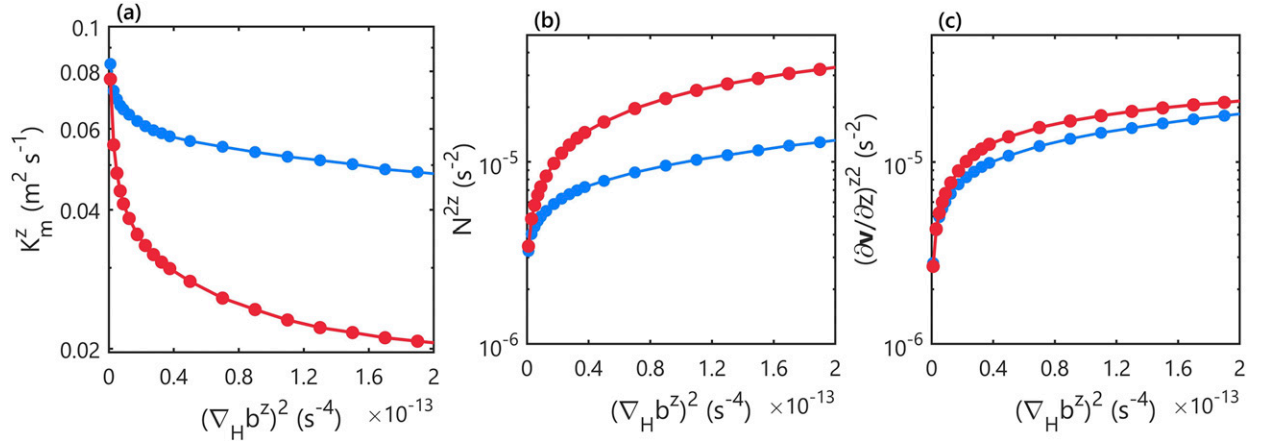


FIG. 7. Bin-averaged (a)  $K_m^z$ , (b)  $N^{2z}$ , and (c)  $(\partial v / \partial z)^2 z$  as a function of  $(\nabla_H b^z)^2$  in the downfront-wind case ( $0^\circ \leq \theta \leq 30^\circ$ ; blue) and upfront-wind case ( $150^\circ \leq \theta \leq 180^\circ$ ; red). The values are derived from NEFB.

suggested by the parameterizations of  $B_f$  for these mechanisms (Fox-Kemper et al. 2008; McWilliams 2016). In fact, the value of  $\langle H \rangle_{s,t}$  in NCFB is 19.5% larger than that in NEFB, largely reconciling the different responses of  $\langle B_f^{qg} \rangle_{s,t}$  and  $\langle (\nabla_H b^z)^2 \rangle_{s,t}$  to the eddy thermal feedback. On the other hand, the weakened stratification in NCFB enhances  $K_m$  (Fig. 8c). The value of  $\langle K_m \rangle_{s,t}$  at its peaking depth is 26.9% larger in NCFB than in NEFB, acting to compensate the decrease of  $\langle B_f^{vm} \rangle_{s,t}$  due to the reduced  $\langle (\nabla_H b^z)^2 \rangle_{s,t}$  in NCFB. We find that such negative feedbacks on  $B_f$  due to  $B_f$ -induced restratification occur almost instantaneous. Even after a few days' model integration, the reduction of  $\langle B_f \rangle_s$  in NCFB than NEFB becomes evidently smaller than that of  $\langle (\nabla_H b^z)^2 \rangle_s$  (Fig. S2). In a word, the eddy thermal feedback reduces  $B_f$  by damping front intensity, but this reduction is

partially offset by the interaction between the stratification and  $B_f$ .

#### b. Eddy current feedback

We evaluate the influence of eddy current feedback on  $B_f$  by comparing the results in CTRL and NCFB. The eddy current feedback results in negative wind power on ocean eddies. This eddy kinetic energy (EKE) dissipation pathway weakens the mean EKE level in the mixed layer by about 40.3% (Fig. 10a). Consistent with Renault et al. (2018), the eddy current feedback has a negligible influence on  $B_f$  despite its evident effect on EKE. The value of  $\langle B_f \rangle_{s,t}$  at its peaking depth is only 1.7% smaller in CTRL than in NCFB (Fig. 11a). Decomposition of  $B_f$  based on the G-GMA omega equation indicates that both  $\langle B_f^{qg} \rangle_{s,t}$  and  $\langle B_f^{vm} \rangle_{s,t}$  are insensitive to the eddy current feedback

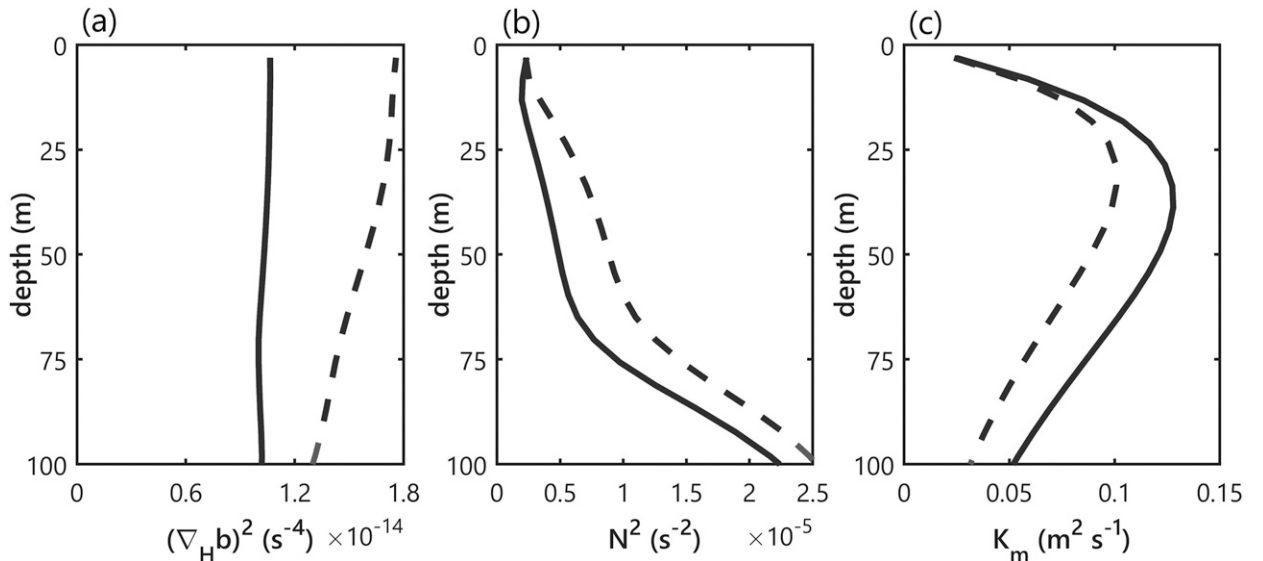


FIG. 8. Vertical profiles of (a)  $\langle (\nabla_H b^z)^2 \rangle_{s,t}$ , (b)  $\langle N^2 \rangle_{s,t}$ , and (c)  $\langle K_m \rangle_{s,t}$  in NCFB (solid) and in NEFB (dashed).

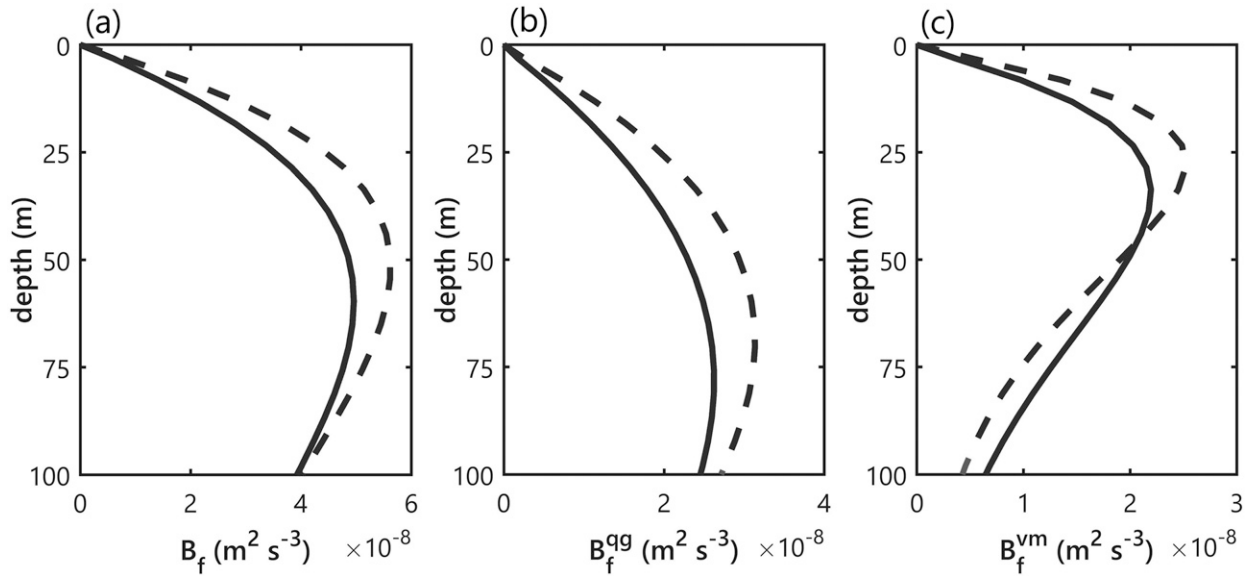


FIG. 9. Vertical profiles of (a)  $\langle B_f \rangle_{s,t}$ , (b)  $\langle B_f^{\text{gg}} \rangle_{s,t}$ , and (c)  $\langle B_f^{\text{vm}} \rangle_{s,t}$  in NCFB (solid) and in NEFB (dashed).

(Figs. 11b,c). In particular, the value of  $\langle B_f^{\text{vm}} \rangle_{s,t}$  in CTRL is almost the same as that in NCFB at its peaking depth.

The differed responses of EKE and  $B_f$  to the eddy current feedback are mainly attributed to the following two facts. First, the eddy current feedback works most effectively at the EKE containing scales (Duhaut and Straub 2006) that are larger than the scales of mixed layer fronts. Indeed, more than 84% of EKE in our simulation is contributed by motions with horizontal wavelengths larger than 100 km, whereas this range only accounts for less than 20% of  $(\nabla_H b)^2$ . Correspondingly,  $(\nabla_H b)^2$  is weakened by the eddy

current feedback to an extent much less evident than EKE (Fig. 10b). In specific, the value of  $\langle (\nabla_H b)^2 \rangle_{s,t}$  is only 13.7% smaller in CTRL than in NCFB.

The second fact is that the eddy current's imprint on wind stress induces wind stress curl anomaly in phase with  $b'$  in the mixed layer (Dewar and Flierl 1987; Klein and Lapeyre 2009; Gaube et al. 2015), producing an upward eddy buoyancy flux through the Ekman pumping (Li et al. 2021). This is evidenced by the positive value of  $\langle B_{f,\tau}^{\text{TTW}} \rangle_{s,t}$  with  $B_{f,\tau}^{\text{TTW}} = w_\tau b'$  in CTRL, whereas it is zero in NCFB (Fig. 11d). Such an effect in CTRL largely compensates the reduction of  $\langle B_f^{\text{TTW}} \rangle_{s,t}$

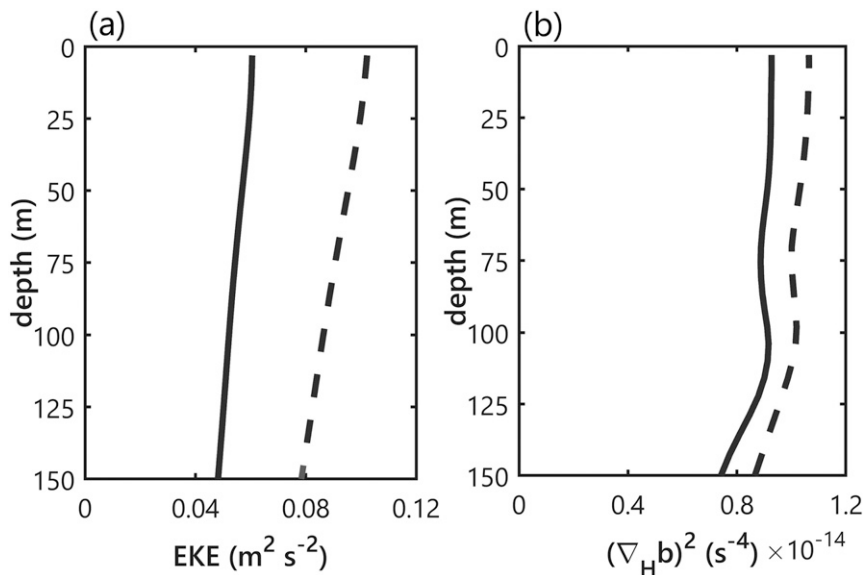


FIG. 10. Vertical profiles of (a)  $\langle \text{EKE} \rangle_{s,t}$  and (b)  $\langle (\nabla_H b)^2 \rangle_{s,t}$  in CTRL (solid) and in NCFB (dashed).

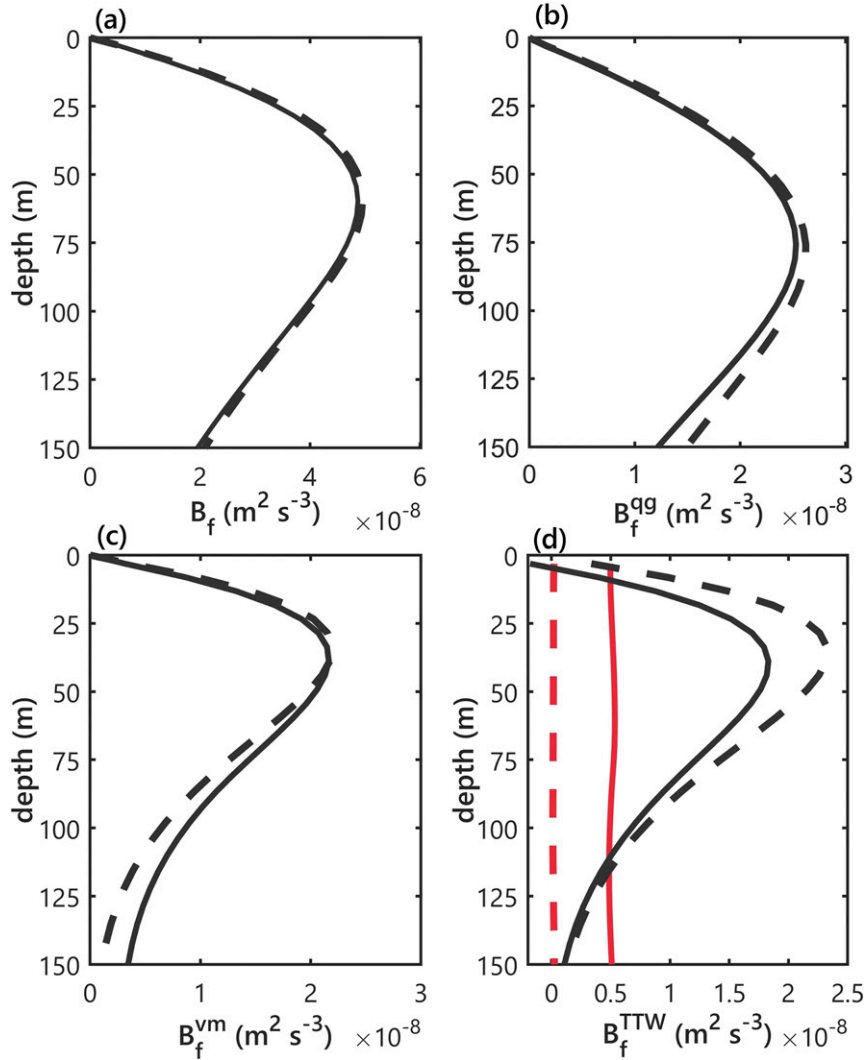


FIG. 11. Vertical profiles of (a)  $\langle B_f \rangle_{s,t}$ , (b)  $\langle B_f^{qg} \rangle_{s,t}$ , (c)  $\langle B_f^{vm} \rangle_{s,t}$ , and (d)  $\langle B_f^{TTW} \rangle_{s,t}$  (red) and  $\langle B_f^{TTW} - B_{f,\tau}^{TTW} \rangle_{s,t}$  (black) in CTRL (solid) and in NCFB (dashed).

caused by the decreased  $\langle B_{f,S}^{TTW} \rangle_{s,t}$  as a result of the weakened mixed layer fronts. This makes the difference of  $\langle B_f \rangle_{s,t}$  between CTRL and NCFB even smaller than that inferred from  $\langle (\nabla_H b)^2 \rangle_{s,t}$ , explaining the insensitivity of  $\langle B_f \rangle_{s,t}$  to the eddy current feedback.

## 5. Discussion

### a. Internal Ekman pumping

This study reveals the key role of TTW balance in transmitting the effects of air–sea interactions on  $B_f$  (and also  $Q_T$ ) in the winter mixed layer. Despite a simple balance among Coriolis force, horizontal pressure gradient and turbulent vertical mixing of momentum, the TTW balance accommodates at least three distinct mechanisms in generating  $B_f$ . The first one is the Ekman pumping induced by the eddy current’s imprint on wind stress curl. The second is related to the ASC

driven by the vertical mixing of geostrophic momentum. This ASC acts to restore the vertical shear against the destruction by turbulent vertical mixing and thus always produces a positive  $B_f$  (McWilliams et al. 2015; Wenegrat and McPhaden 2016). The third, which has not been systematically documented elsewhere to the best of our knowledge,<sup>6</sup> is due to the difference of  $K_m$  between the front center and periphery. As the horizontal ageostrophic flows in the third mechanism are governed by the classical Ekman equation yet the associated vertical velocity is essentially ascribed to the horizontal

<sup>6</sup> We note that there are a few studies adopting a horizontally varying  $K_m$  when modelling the vertical velocity in the Ekman layer (e.g., Nagai et al. 2006; McWilliams et al. 2015; Wenegrat and McPhaden 2016). But its importance for generated  $Q_T$  has not been explicitly explored in these studies.

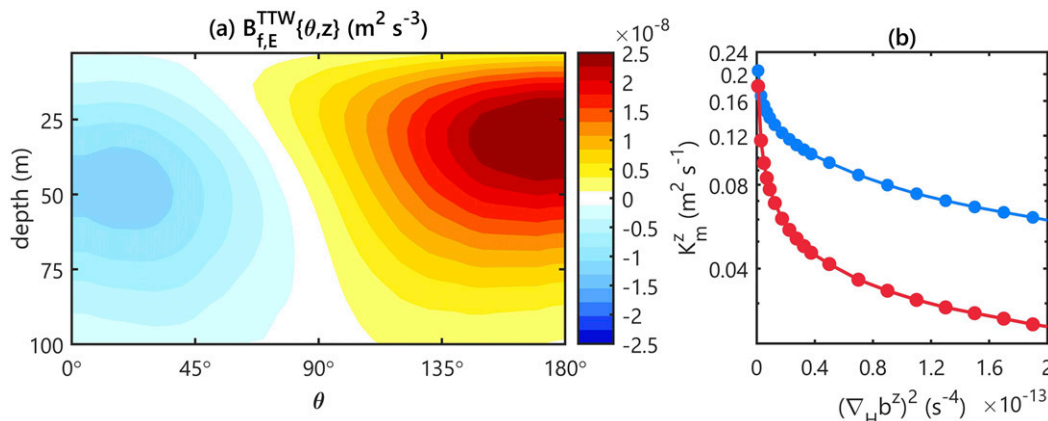


FIG. 12. (a) Distribution of  $B_{f,E}^{TTW}\{\theta, z\}$  in the MY25 run. (b) Bin-averaged  $K_m^z$  as a function of  $(\nabla_H b^z)^2$  in the downfront-wind case ( $0^\circ \leq \theta \leq 30^\circ$ ; blue) and upfront-wind case ( $150^\circ \leq \theta \leq 180^\circ$ ; red) in the MY25 run.

inhomogeneity of  $K_m$  in the Ekman layer rather than that of wind stress, we name it the *internal Ekman pumping* to distinguish it from the classical Ekman pumping. Unlike the classical Ekman pumping, the vertical velocity of the internal Ekman pumping peaks within the Ekman layer but vanishes at the layer base. Moreover, although the classical Ekman pumping caused by the eddy current's imprint on wind stress curl always results in a positive  $B_f$ , the sign of  $B_f$  generated by the internal Ekman pumping depends tightly on the direction of wind stress relative to fronts and horizontal structure of  $K_m$ . For smaller  $K_m$  at the front center than periphery as in our simulation, it is positive and negative under the upfront- and downfront-wind forcing, respectively. However, due to its magnitude asymmetry between upfront- and downfront-wind forcing (Figs. 4d and 6), the internal Ekman pumping is supposed to contribute to a net upward buoyancy flux. The net contribution of the internal Ekman pumping can be estimated from  $\langle B_{f,E}^{TTW} \rangle_{s,t}$  in NCFB as the eddy current's imprint on wind stress curl is removed in this experiment. Consistent with our conjecture, the value of  $\langle B_{f,E}^{TTW} \rangle_{s,t}$  in NCFB is positive definite with its peaking magnitude  $3 \times 10^{-9} \text{ m}^2 \text{ s}^{-3}$  about 60% of  $\langle B_{f,\tau}^{TTW} \rangle_{s,t}$  in CTRL. It thus suggests that the internal Ekman pumping and classical Ekman pumping through the eddy current feedback make comparable contribution to the temporally and/or spatially averaged  $B_f$ .

Finally, there is a caveat on the universality of the smaller  $K_m$  at the front center than periphery reported in this study, as it is derived based on a particular mixing parameterization scheme (i.e., the KPP) in a particular region (i.e., the winter Kuroshio extension). To examine the uncertainties resulting from the mixing parameterizations, we perform another simulation with the same setting as NEFB but replace the KPP scheme with the Mellor–Yamada level 2.5 turbulence closure scheme (Mellor and Yamada 1974, 1982; referred to as the MY25 scheme for short). It is found that the dependence of  $B_{f,E}^{TTW}\{\theta, z\}$  on  $\theta$  in the MY25 run (Fig. 12a) is qualitatively similar to that in the KPP run (Fig. 4d). In particular,  $B_{f,E}^{TTW}\{\theta, z\}$  in the MY25 run is characterized by a dipolar mode as in the KPP run, being strongly positive and weakly negative

in the upfront- and downfront-wind cases, respectively. In addition, consistent with the KPP run, the value of  $K_m^z$  in the MY25 run exhibits a decreasing trend with  $(\nabla_H b^z)^2$  (Fig. 12b). It thus suggests that the reduced  $K_m$  at the front center than periphery also holds for the MY25 scheme and is unlikely to be an artifact produced by the KPP scheme. Nevertheless, observations of horizontal structure of  $K_m$  in the frontal regions are necessary to make further validation. It should be noted that direct measurements of  $K_m$  are still challenging at present. So far, existing observations in the frontal regions have been mostly conducted for the turbulent kinetic dissipation rate (e.g., D'Asaro et al. 2011; Fer and Drinkwater 2014; Koenig et al. 2020). Yet the large difference of vertical shear variance between the front center and periphery makes it difficult to infer the horizontal structure of  $K_m$  from that of turbulent kinetic dissipation rate alone (Osborn 1974). Moreover, the coincidence of strong ocean eddies and atmosphere storms makes the winter Kuroshio extension dynamically distinctive from the basin interior and eastern boundary current regions. It remains unclear whether the reduced  $K_m$  at the front center than periphery also holds in the other parts of the global ocean but deserves further studies.

#### b. Nonlinear Ekman pumping

In this study, we do not consider the nonlinear Ekman pumping explicitly because it becomes intractable when the Rossby number and Ekman number both become finite as in our 1-km simulation (Stern 1965; Niiler 1969; Thomas and Lee 2005; Wenegrat and Thomas 2017). The nonlinear Ekman pumping can affect  $B_f$  (and also  $Q_\tau$ ) in different ways. First, it may contribute to  $B_f$  directly through its induced vertical velocity. However, this effect seems negligible as we have shown in Part I that  $\langle B_f \rangle_s$  is mostly accounted for by the geostrophic deformation and TTW balance. We note that the negligible role of nonlinear Ekman pumping on  $B_f$  is consistent with a recent study by Li et al. (2021). Second, as suggested by Thomas and Lee (2005), the nonlinear Ekman pumping may indirectly affect  $B_f$  by promoting the frontogenesis and turbulent vertical mixing in the downfront-wind case. However, as



revealed by Fig. 4a, the magnitude of  $(\nabla_H b)^2$  changes by less than 20% for all the wind directions and is reduced in the upfront-wind forcing. This suggests that the effect of nonlinear Ekman pumping on  $B_f$  between the downfront- and upfront-wind case might largely cancel each other, making little net contribution to  $\langle B_f \rangle_s$ . Nevertheless, by enhancing  $(\nabla_H b)^2$  and  $K_m$  in the downfront-wind case and reducing them in the upfront-wind case, the nonlinear Ekman pumping does play a role in shaping the dependence of  $B_f$  on the wind direction (Figs. 3 and 4).

### c. Limitation for using uncoupled ocean simulations

Ideally, the effects of air–sea interactions on  $B_f$  (and also  $Q_T$ ) should be analyzed based on coupled simulations that are currently difficult to accomplish due to the large computation burden at submesoscale resolution. Although computationally feasible, uncoupled ocean simulations are deficient in representing the eddy thermal and current feedbacks as the overlying atmosphere is not allowed to adjust to the eddies' imprint on the heat, freshwater, and momentum exchanges at the air–sea interface. Yang et al. (2018) reported that neglecting the atmosphere's adjustment would overestimate the eddy thermal feedback by 20%–40% in the Kuroshio extension. Estimates for the influence of atmosphere's adjustment to eddy current feedback in this region are still absent. As a reference, Renault et al. (2016) found an overestimation of EKE attenuation due to the eddy current feedback by  $\sim 30\%$  in the California Current System. These findings suggest that the eddy thermal and current feedbacks are moderately overestimated in our uncoupled simulations and probably so are their effects on  $B_f$ . Nevertheless, such overestimation is unlikely to qualitatively alter the major conclusions in this study.

In addition to the eddy thermal and current feedbacks, SST anomalies carried by eddies in the winter Kuroshio extension regulate the surface wind speed through the vertical mixing mechanism (Nonaka and Xie 2003; Xie 2004; Small et al. 2008). Specifically, surface wind speed tends to be enhanced (weakened) over the warm (cold) SST anomaly. This kind of eddy–atmosphere interaction is not included in our ocean-alone simulation. Existing literature suggests that it affects the eddy propagation but has no significant influences on eddy energetics, as the resultant wind stress curl anomaly is out of phase with the SST anomalies carried by eddies (Dewar and Flierl 1987; Small et al. 2008; Gaube et al. 2015; Seo et al. 2016). Therefore, we conjecture that the imprint of eddy-induced SST anomalies on surface wind speed should have negligible effects on  $B_f$ . However, fully coupled simulations are necessary to test this conjecture.

## 6. Conclusions

In this study, we analyze the regulation of vertical eddy heat transport  $Q_T$  within the winter mixed layer of the Kuroshio extension by the air–sea interactions. Effects of three different kinds of air–sea interactions are presented, i.e., the atmosphere synoptic forcing, eddy thermal, and current feedbacks. To facilitate dynamic analyses, we use the vertical eddy buoyancy flux  $B_f$  as a proxy for  $Q_T$ . As the buoyancy change is dominated by the temperature change in the winter Kuroshio extension,

all the major conclusions on the effects of air–sea interactions on  $B_f$  listed as follows hold for  $Q_T$ .

- 1) Variation of  $B_f$  at the intraseasonal time scales is strongly regulated by the surface heat flux and wind stress magnitude by affecting the  $B_f$  component contributed by the turbulent thermal wind (TTW) balance  $B_f^{\text{TTW}}$ . Strong surface cooling associated with intense winds enhances the destruction of vertical shear by turbulent vertical mixing, inducing a stronger ageostrophic secondary circulation (ASC) to restore the vertical shear and thus promoting  $B_f$ .
- 2) Intensity of  $B_f$  is also affected by the direction of wind stress relative to that of mixed layer fronts via  $B_f^{\text{TTW}}$ , exhibiting enhancement both under the downfront- and upfront-wind forcing. On one hand, the downfront-wind forcing enhances the turbulent vertical viscosity through the destabilizing wind-driven Ekman buoyancy flux and front intensity through the frontogenesis, triggering a stronger ASC to restore the vertical shear against the destruction by turbulent vertical mixing and intensifying  $B_f^{\text{TTW}}$ . On the other hand, the interaction of uniform wind stress with smaller turbulent vertical viscosity at the front center than periphery (i.e., the internal Ekman pumping) produces an upward buoyancy transport under the upfront-wind forcing, accounting for the enhanced  $B_f^{\text{TTW}}$  in the upfront-wind case.
- 3) By weakening fronts in the mixed layer, the eddy thermal feedback reduces  $B_f$  contributed by the geostrophic deformation and TTW. The value of  $B_f$  at its peaking depth is 12% smaller in the simulation with the eddy thermal feedback than otherwise. However, such reduction is much less evident than that of  $(\nabla_H b)^2$ , i.e., 34%. The discrepancy is mainly due to the restratification effect of  $B_f$  and its negative feedback on  $B_f$  itself. The mixed layer depth and turbulent vertical viscosity are significantly increased in the presence of the eddy thermal feedback due to the reduced  $B_f$ , reconciling the differed responses of  $B_f$  and  $(\nabla_H b)^2$  to the eddy thermal feedback.
- 4) The eddy current feedback has little influence on  $B_f$ , although it weakens EKE in the mixed layer by 40%. The differed responses of  $B_f$  and EKE are partially because mixed layer fronts have smaller horizontal scales than the EKE containing scales and are thus damped by the eddy current feedback to a much less extent. Furthermore, the eddy current's imprint on wind stress generates an upward eddy buoyancy transport through the Ekman pumping, compensating the reduced  $B_f$  due to the slightly weakened mixed layer fronts by the eddy current feedback.

The winter Kuroshio extension is one of the major formation sites of the mode water that is characterized by anomalous low potential vorticity (PV) and plays a crucial role in the basin-scale ocean circulation and climate variability (Hanawa and Talley 2001; Qiu 2002; Oka et al. 2007). As suggested by the impermeability theorem (Haynes and McIntyre 1987, 1990), the volume-integrated PV between two isopycnal layers changes only in response to the diabatic and viscous effects at the surface outcropping area, suggesting that the PV changes are largely controlled by the air–sea

buoyancy and momentum exchanges. However, it does not mean that  $B_f$  plays no role in the PV changes, as it is the convergence of turbulent vertical buoyancy and momentum fluxes rather the fluxes themselves at the surface that are related to the surface PV flux (Thomas 2005; Taylor and Ferrari 2010; Wenegrat et al. 2018). Through regulating the stratification and thus turbulent vertical viscosity in the mixed layer,  $B_f$  can affect the PV changes indirectly. In this study, we demonstrate that the surface buoyancy and momentum fluxes, either driven by atmospheric synoptic variabilities or ocean eddies, have evident impacts on  $B_f$ . It thus implies complicated effects of different kinds of air–sea interactions on PV changes. A better knowledge of these effects will be essential for understanding the mode water formation and destruction processes, which requires further study.

**Acknowledgments.** This research is supported by National Science Foundation of China (41822601, 41776006), Taishan Scholar Funds (tsqn201909052), Fundamental Research Funds for the Central Universities (202072009), and the Marine S&T Fund of Shandong Province for Pilot National Laboratory for Marine Science and Technology (Qingdao) (2018SDKJ0102). The model simulation and many of the computations were executed at the High Performance Computing Center of Pilot National Laboratory for Marine Science and Technology (Qingdao). We would like to acknowledge supports from the International Laboratory for High-Resolution Earth System Prediction, a collaboration by Pilot National Laboratory for Marine Science and Technology, Texas A&M University, and the U.S. National Center for Atmospheric Research.

## APPENDIX

### Expression of G-GMA Omega Equation

The GMA equations for horizontal momentum and buoyancy generalized to include diabatic and viscous effects are

$$\frac{\partial u_g}{\partial t} + u \frac{\partial u_g}{\partial x} + v \frac{\partial u_g}{\partial y} + w \frac{\partial u_g}{\partial z} = f v_a + D_V(u) + D_H(u), \quad (\text{A1a})$$

$$\frac{\partial v_g}{\partial t} + u \frac{\partial v_g}{\partial x} + v \frac{\partial v_g}{\partial y} + w \frac{\partial v_g}{\partial z} = -f u_a + D_V(v) + D_H(v), \quad (\text{A1b})$$

$$\frac{\partial b}{\partial t} + u \frac{\partial b}{\partial x} + v \frac{\partial b}{\partial y} + w \frac{\partial b}{\partial z} = D_V(b), \quad (\text{A1c})$$

$$\frac{\partial u_a}{\partial x} + \frac{\partial v_a}{\partial y} + \frac{\partial w}{\partial z} = 0, \quad (\text{A1d})$$

where  $p$  is the pressure,  $D_V(u)/D_V(v)$  is the vertical mixing for zonal/meridional momentum,  $D_H(u)/D_H(v)$  is the horizontal mixing for zonal/meridional momentum, and  $D_V(b)$  is the vertical mixing for buoyancy. To obtain Eq. (A1d), we drop the term proportional to the meridional derivative of  $f$ .

As demonstrated in Part I, the explicit expressions for each term on the rhs of Eq. (6) are

$$\begin{aligned} F_{\text{qg}} &= -2\nabla_H \cdot \left( \frac{\partial \mathbf{v}_g}{\partial x} \cdot \nabla_H b, \frac{\partial \mathbf{v}_g}{\partial y} \cdot \nabla_H b \right), \\ F_{\text{ag}} &= \nabla_H \cdot \left( f \frac{\partial \mathbf{v}_a}{\partial z} \cdot \nabla_H v_g - f \frac{\partial \mathbf{v}_g}{\partial z} \cdot \nabla_H v_a - 2 \frac{\partial \mathbf{v}_a}{\partial x} \cdot \nabla_H b, \right. \\ &\quad \left. - f \frac{\partial \mathbf{v}_a}{\partial z} \cdot \nabla_H u_g + f \frac{\partial \mathbf{v}_g}{\partial z} \cdot \nabla_H u_a - 2 \frac{\partial \mathbf{v}_a}{\partial y} \cdot \nabla_H b \right), \\ F_{\text{vm}} &= -f \frac{\partial}{\partial z} \left[ \frac{\partial D_V(v)}{\partial x} - \frac{\partial D_V(u)}{\partial y} \right], \\ F_{\text{hm}} &= -f \frac{\partial}{\partial z} \left[ \frac{\partial D_H(v)}{\partial x} - \frac{\partial D_H(u)}{\partial y} \right], \\ F_{\text{vb}} &= \nabla_H^2 [D_V(b)]. \end{aligned}$$

## REFERENCES

- Allen, J. T., D. A. Smeed, A. J. G. Nurser, J. W. Zhang, and M. Rixen, 2001: Diagnosis of vertical velocities with the QG omega equation: An examination of the errors due to sampling strategy. *Deep-Sea Res. I*, **48**, 315–346, [https://doi.org/10.1016/S0967-0637\(00\)00035-2](https://doi.org/10.1016/S0967-0637(00)00035-2).
- Bishop, S., R. Small, F. Bryan, and R. Tomas, 2017: Scale dependence of midlatitude air–sea interaction. *J. Climate*, **30**, 8207–8221, <https://doi.org/10.1175/JCLI-D-17-0159.1>.
- Callies, J., and R. Ferrari, 2018: Baroclinic instability in the presence of convection. *J. Phys. Oceanogr.*, **48**, 45–60, <https://doi.org/10.1175/JPO-D-17-0028.1>.
- , —, J. M. Klymak, and J. Gula, 2015: Seasonality in sub-mesoscale turbulence. *Nat. Commun.*, **6**, 6862, <https://doi.org/10.1038/ncomms7862>.
- Capet, X., J. C. McWilliams, M. J. Molemaker, and A. F. Shchepetkin, 2008: Mesoscale to submesoscale transition in the California Current System. Part II: Frontal processes. *J. Phys. Oceanogr.*, **38**, 44–64, <https://doi.org/10.1175/2007JPO3672.1>.
- Chelton, D. B., 2004: Satellite measurements reveal persistent small-scale features in ocean winds. *Science*, **303**, 978–983, <https://doi.org/10.1126/science.1091901>.
- Cronin, M. F., and W. S. Kessler, 2009: Near-surface shear flow in the tropical Pacific cold tongue front. *J. Phys. Oceanogr.*, **39**, 1200–1215, <https://doi.org/10.1175/2008JPO4064.1>.
- , and Coauthors, 2010: Monitoring ocean–atmosphere interactions in western boundary current extensions. *Proc. of OceanObs'09: Sustained Ocean Observations and Information for Society*, Venice, Italy, European Space Agency, 199–209, <http://www.oceanobs09.net/proceedings/cwp/cwp20>.
- D'Asaro, E., C. Lee, L. Rainville, R. Harcourt, and L. Thomas, 2011: Enhanced turbulence and energy dissipation at ocean fronts. *Science*, **332**, 318–322, <https://doi.org/10.1126/science.1201515>.
- Dawe, J. T., and L. Thompson, 2006: Effect of ocean surface currents on wind stress, heat flux, and wind power input to the ocean. *Geophys. Res. Lett.*, **33**, L09604, <https://doi.org/10.1029/2006GL025784>.
- Dewar, W., and G. Flierl, 1987: Some effects of the wind on rings. *J. Phys. Oceanogr.*, **17**, 1653–1667, [https://doi.org/10.1175/1520-0485\(1987\)017<1653:SEOTWO>2.0.CO;2](https://doi.org/10.1175/1520-0485(1987)017<1653:SEOTWO>2.0.CO;2).
- Duhaut, T., and D. Straub, 2006: Wind stress dependence on ocean surface velocity: Implications for mechanical energy input to ocean circulation. *J. Phys. Oceanogr.*, **36**, 202–211, <https://doi.org/10.1175/JPO2842.1>.
- Ekman, V. W., 1905: On the influence of the earth's rotation on ocean currents. *Arch. Math. Astron. Phys.*, **2**, 1–52.

- Fer, I., and K. Drinkwater, 2014: Mixing in the Barents Sea polar front near Hopen in spring. *J. Mar. Syst.*, **130**, 206–218, <https://doi.org/10.1016/j.jmarsys.2012.01.005>.
- Fox-Kemper, B., R. Ferrari, and R. Hallberg, 2008: Parameterization of mixed layer eddies. Part I: Theory and diagnosis. *J. Phys. Oceanogr.*, **38**, 1145–1165, <https://doi.org/10.1175/2007JPO3792.1>.
- Garrett, C. J. R., and J. W. Loder, 1981: Dynamical aspects of shallow sea fronts. *Philos. Trans. Roy. Soc. London*, **302A**, 563–581, <https://doi.org/10.1098/rsta.1981.0183>.
- Gaube, P., D. B. Chelton, R. M. Samelson, M. G. Schlax, and L. W. O'Neill, 2015: Satellite observations of mesoscale eddy-induced Ekman pumping. *J. Phys. Oceanogr.*, **45**, 104–132, <https://doi.org/10.1175/JPO-D-14-0032.1>.
- Griffies, S. M., and R. W. Hallberg, 2000: Biharmonic friction with a Smagorinsky-like viscosity for use in large-scale eddy-permitting ocean models. *Mon. Wea. Rev.*, **128**, 2935–2946, [https://doi.org/10.1175/1520-0493\(2000\)128<2935:BFWASL>2.0.CO;2](https://doi.org/10.1175/1520-0493(2000)128<2935:BFWASL>2.0.CO;2).
- Gula, J., M. J. Molemaker, and J. C. McWilliams, 2014: Submesoscale cold filaments in the gulf stream. *J. Phys. Oceanogr.*, **44**, 2617–2643, <https://doi.org/10.1175/JPO-D-14-0029.1>.
- Haidvogel, D. B., H. G. Arango, K. Hedstrom, A. Beckmann, P. Malanotte-Rizzoli, and A. F. Shchepetkin, 2000: Model evaluation experiments in the North Atlantic basin: Simulations in nonlinear terrain-following coordinates. *Dyn. Atmos. Oceans*, **32**, 239–281, [https://doi.org/10.1016/S0377-0265\(00\)00049-X](https://doi.org/10.1016/S0377-0265(00)00049-X).
- Hanawa, K., and L. D. Talley, 2001: Mode waters. *Ocean Circulation and Climate*, G. Siedler, J. Church, and J. Gould, Eds., International Geophysics Series, Vol. 77, Academic Press, 373–386.
- Hausmann, U., A. Czaja, and J. Marshall, 2016: Estimates of air–sea feedbacks on sea surface temperature anomalies in the southern ocean. *J. Climate*, **29**, 439–454, <https://doi.org/10.1175/JCLI-D-15-0015.1>.
- Haynes, P. H., and M. E. McIntyre, 1987: On the evolution of vorticity and potential vorticity in the presence of diabatic heating and frictional or other forces. *J. Atmos. Sci.*, **44**, 828–841, [https://doi.org/10.1175/1520-0469\(1987\)044<0828:OTEOVA>2.0.CO;2](https://doi.org/10.1175/1520-0469(1987)044<0828:OTEOVA>2.0.CO;2).
- , and —, 1990: On the conservation and impermeability theorems for potential vorticity. *J. Atmos. Sci.*, **47**, 2021–2031, [https://doi.org/10.1175/1520-0469\(1990\)047<2021:OTCAIT>2.0.CO;2](https://doi.org/10.1175/1520-0469(1990)047<2021:OTCAIT>2.0.CO;2).
- Klein, P., and G. Lapeyre, 2009: The oceanic vertical pump induced by mesoscale and submesoscale turbulence. *Annu. Rev. Mar. Sci.*, **1**, 351–375, <https://doi.org/10.1146/annurev.marine.010908.163704>.
- Koenig, Z., I. Fer, E. Kolås, T. O. Fossum, P. Norgren, and M. Ludvigsen, 2020: Observations of turbulence at a near-surface temperature front in the Arctic Ocean. *J. Geophys. Res. Oceans*, **125**, e2019JC015526, <https://doi.org/10.1029/2019JC015526>.
- Large, W. G., and S. Yeager, 2004: Diurnal to decadal global forcing for ocean and sea-ice models: The data sets and flux climatologies. NCAR Tech. Note NCAR/TN-460+STR, 105 pp., <https://doi.org/10.5065/D6KK98Q6>.
- , J. C. McWilliams, and S. C. Doney, 1994: Oceanic vertical mixing: A review and a model with a nonlocal boundary layer parameterization. *Rev. Geophys.*, **32**, 363–403, <https://doi.org/10.1029/94RG01872>.
- Li, D., P. Chang, S. Ramachandran, Z. Jing, Q. Zhang, J. Kurian, A. Gopal, and H. Yang, 2021: Contribution of the two types of Ekman pumping induced eddy heat flux to the total vertical eddy heat flux. *Geophys. Res. Lett.*, **48**, e2021GL092982, <https://doi.org/10.1029/2021GL092982>.
- Ma, X., and Coauthors, 2016: Western boundary currents regulated by interaction between ocean eddies and the atmosphere. *Nature*, **535**, 533–537, <https://doi.org/10.1038/nature18640>.
- Mahadevan, A., A. Tandon, and R. Ferrari, 2010: Rapid changes in mixed layer stratification driven by submesoscale instabilities and winds. *J. Geophys. Res.*, **115**, C03017, <https://doi.org/10.1029/2008JC005203>.
- Marshall, J., and F. Schott, 1999: Open-ocean convection: Observations, theory, and models. *Rev. Geophys.*, **37**, 1–64, <https://doi.org/10.1029/98RG02739>.
- McWilliams, J. C., 2016: Submesoscale currents in the ocean. *Proc. Roy. Soc.*, **A472**, 20160117, <https://doi.org/10.1098/rspa.2016.0117>.
- , 2017: Submesoscale surface fronts and filaments: Secondary circulation, buoyancy flux, and frontogenesis. *J. Fluid Mech.*, **823**, 391–432, <https://doi.org/10.1017/jfm.2017.294>.
- , J. Gula, M. J. Molemaker, L. Renault, and A. F. Shchepetkin, 2015: Filament frontogenesis by boundary layer turbulence. *J. Phys. Oceanogr.*, **45**, 1988–2005, <https://doi.org/10.1175/JPO-D-14-0211.1>.
- Mellor, G. L., and T. Yamada, 1974: A hierarchy of turbulence closure models for planetary boundary layers. *J. Atmos. Sci.*, **31**, 1791–1806, [https://doi.org/10.1175/1520-0469\(1974\)031<1791:AHOTCM>2.0.CO;2](https://doi.org/10.1175/1520-0469(1974)031<1791:AHOTCM>2.0.CO;2).
- , and —, 1982: Development of a turbulence closure model for geophysical fluid problems. *Rev. Geophys.*, **20**, 851–875, <https://doi.org/10.1029/RG020i004p00851>.
- Nagai, T., A. Tandon, and D. L. Rudnick, 2006: Two-dimensional ageostrophic secondary circulation at ocean fronts due to vertical mixing and large-scale deformation. *J. Geophys. Res.*, **111**, C09038, <https://doi.org/10.1029/2005JC002964>.
- Niiler, P. P., 1969: On the Ekman divergence in an oceanic jet. *J. Geophys. Res.*, **74**, 7048–7052, <https://doi.org/10.1029/JC074i028p07048>.
- Nonaka, M., and S.-P. Xie, 2003: Covariations of sea surface temperature and wind over the Kuroshio and its extension: Evidence for ocean-to-atmosphere feedback. *J. Climate*, **16**, 1404–1413, [https://doi.org/10.1175/1520-0442\(2003\)16<1404:COSSA>2.0.CO;2](https://doi.org/10.1175/1520-0442(2003)16<1404:COSSA>2.0.CO;2).
- Oka, E., L. D. Talley, and T. Suga, 2007: Temporal variability of winter mixed layer in the mid-to high-latitude North Pacific. *J. Oceanogr.*, **63**, 293–307, <https://doi.org/10.1007/s10872-007-0029-2>.
- Ortega, J. M., and W. C. Rheinboldt, 2014: *Iterative Solution of Nonlinear Equations in Several Variables*. Elsevier, 593 pp.
- Osborn, T. R., 1974: Vertical profiling of velocity microstructure. *J. Phys. Oceanogr.*, **4**, 109–115, [https://doi.org/10.1175/1520-0485\(1974\)004<0109:VPOVM>2.0.CO;2](https://doi.org/10.1175/1520-0485(1974)004<0109:VPOVM>2.0.CO;2).
- Press, W. H., S. A. Teukolsky, B. P. Flannery, and W. T. Vetterling, 1992: *Numerical Recipes in Fortran 77: The Art of Scientific Computing*. Cambridge University Press, 973 pp.
- Qiu, B., 2002: The Kuroshio extension system: Its large-scale variability and role in the midlatitude ocean-atmosphere interaction. *J. Oceanogr.*, **58**, 57–75, <https://doi.org/10.1023/A:1015824717293>.
- Renault, L., M. J. Molemaker, J. C. McWilliams, A. F. Shchepetkin, F. Lemarié, D. Chelton, S. Illig, and A. Hall, 2016: Modulation of wind work by oceanic current interaction with the atmosphere. *J. Phys. Oceanogr.*, **46**, 1685–1704, <https://doi.org/10.1175/JPO-D-15-0232.1>.
- , J. C. McWilliams, and J. Gula, 2018: Dampening of submesoscale currents by air–sea stress coupling in the Californian upwelling system. *Sci. Rep.*, **8**, 13388, <https://doi.org/10.1038/s41598-018-31602-3>.
- Saha, S., and Coauthors, 2010: The NCEP Climate Forecast System Reanalysis. *Bull. Amer. Meteor. Soc.*, **91**, 1015–1058, <https://doi.org/10.1175/2010BAMS3001.1>.
- Sasaki, H., P. Klein, B. Qiu, and Y. Sasai, 2014: Impact of oceanic-scale interactions on the seasonal modulation of

- ocean dynamics by the atmosphere. *Nat. Commun.*, **5**, 5636, <https://doi.org/10.1038/ncomms6636>.
- , —, Y. Sasai, and B. Qiu, 2017: Regionality and seasonality of submesoscale and mesoscale turbulence in the North Pacific Ocean. *Ocean Dyn.*, **67**, 1195–1216, <https://doi.org/10.1007/s10236-017-1083-y>.
- Seo, H., A. J. Miller, and J. R. Norris, 2016: Eddy–wind interaction in the California Current System: Dynamics and impacts. *J. Phys. Oceanogr.*, **46**, 439–459, <https://doi.org/10.1175/JPO-D-15-0086.1>.
- Shan, X., and Coauthors, 2020a: Surface heat flux induced by mesoscale eddies cools the Kuroshio-Oyashio extension region. *Geophys. Res. Lett.*, **47**, e2019GL086050, <https://doi.org/10.1029/2019GL086050>.
- , Z. Jing, B. Sun, P. P. Chang, L. Wu, and X. Ma, 2020b: Influence of the ocean mesoscale eddy–atmosphere thermal feedback on the upper-ocean haline stratification. *J. Phys. Oceanogr.*, **50**, 2475–2490, <https://doi.org/10.1175/JPO-D-19-0193.1>.
- Shchepetkin, A. F., and J. C. McWilliams, 2005: The Regional Oceanic Modeling System (ROMS): A split-explicit, free-surface, topography-following-coordinate oceanic model. *Ocean Modell.*, **9**, 347–404, <https://doi.org/10.1016/j.ocemod.2004.08.002>.
- Smagorinsky, J., 1963: General circulation experiments with the primitive equations: I. The basic experiment. *Mon. Wea. Rev.*, **91**, 99–164, [https://doi.org/10.1175/1520-0493\(1963\)091<0099:GCEWTP>2.3.CO;2](https://doi.org/10.1175/1520-0493(1963)091<0099:GCEWTP>2.3.CO;2).
- Small, R. J., and Coauthors, 2008: Air–sea interaction over ocean fronts and eddies. *Dyn. Atmos. Oceans*, **45**, 274–319, <https://doi.org/10.1016/j.dynatmoce.2008.01.001>.
- Stern, M. E., 1965: Interaction of a uniform wind stress with a geostrophic vortex. *Deep-Sea Res. Oceanogr. Abstr.*, **12**, 355–367, [https://doi.org/10.1016/0011-7471\(65\)90007-0](https://doi.org/10.1016/0011-7471(65)90007-0).
- Taylor, J. R., and R. Ferrari, 2010: Buoyancy and wind-driven convection at mixed layer density fronts. *J. Phys. Oceanogr.*, **40**, 1222–1242, <https://doi.org/10.1175/2010JPO4365.1>.
- Thomas, L. N., 2005: Destruction of potential vorticity by winds. *J. Phys. Oceanogr.*, **35**, 2457–2466, <https://doi.org/10.1175/JPO2830.1>.
- Thomas, L., and R. Ferrari, 2008: Friction, frontogenesis, and the stratification of the surface mixed layer. *J. Phys. Oceanogr.*, **38**, 2501–2518, <https://doi.org/10.1175/2008JPO3797.1>.
- Thomas, L. N., and C. M. Lee, 2005: Intensification of ocean fronts by down-front winds. *J. Phys. Oceanogr.*, **35**, 1086–1102, <https://doi.org/10.1175/JPO2737.1>.
- , A. Tandon, and A. Mahadevan, 2008: Submesoscale processes and dynamics. *Ocean Modeling in an Eddy Regime*, *Geophys. Monogr.*, Vol. 177, Amer. Geophys. Union, 17–38.
- Thompson, L., 2000: Ekman layers and two-dimensional frontogenesis in the upper ocean. *J. Geophys. Res.*, **105**, 6437–6451, <https://doi.org/10.1029/1999JC900336>.
- Vallis, G. K., 2006: *Atmospheric and Oceanic Fluid Dynamics: Fundamentals and Large-Scale Circulation*. Cambridge University Press, 773 pp.
- Wenegrat, J. O., and M. J. McPhaden, 2016: Wind, waves, and fronts: Frictional effects in a generalized Ekman model. *J. Phys. Oceanogr.*, **46**, 371–394, <https://doi.org/10.1175/JPO-D-15-0162.1>.
- , and L. N. Thomas, 2017: Ekman transport in balanced currents with curvature. *J. Phys. Oceanogr.*, **47**, 1189–1203, <https://doi.org/10.1175/JPO-D-16-0239.1>.
- , —, J. Gula, and J. C. McWilliams, 2018: Effects of the submesoscale on the potential vorticity budget of ocean mode waters. *J. Phys. Oceanogr.*, **48**, 2141–2165, <https://doi.org/10.1175/JPO-D-17-0219.1>.
- Xie, S.-P., 2004: Satellite observations of cool ocean–atmosphere interaction. *Bull. Amer. Meteor. Soc.*, **85**, 195–208, <https://doi.org/10.1175/BAMS-85-2-195>.
- Yang, P., Z. Jing, and L. Wu, 2018: An assessment of representation of oceanic mesoscale eddy–atmosphere interaction in the current generation of general circulation models and reanalyses. *Geophys. Res. Lett.*, **45**, 11 856–11 865, <https://doi.org/10.1029/2018GL080678>.
- Yang, H., P. Chang, B. Qiu, Q. Zhang, L. Wu, Z. Chen, and H. Wang, 2019: Mesoscale air–sea interaction and its role in eddy energy dissipation in the Kuroshio extension. *J. Climate*, **32**, 8659–8676, <https://doi.org/10.1175/JCLI-D-19-0155.1>.
- Yang, P., Z. Jing, B. Sun, L. Wu, B. Qiu, P. Chang, and S. Ramachandran, 2021: On the upper-ocean vertical eddy heat transport in the Kuroshio extension. Part I: Variability and dynamics. *J. Phys. Oceanogr.*, **51**, 229–246, <https://doi.org/10.1175/JPO-D-20-0068.1>.